Am J Cancer Res 2024;14(10):4686-4707
www.ajcr.us /ISSN:2156-6976/ajcr0157311

Original Article

Comprehensive analysis of ferroptosis-related genes indicates that TRIM46 is a novel biomarker and promotes the progression of ovarian cancer via modulating ferroptosis and Wnt signaling pathway

Shuang Liu[1], Chunmei Xiao[1], Yue Rong[1], Mingbo Liu[2], Ke Yang[3], Jing Tang[1], Zhigang Wang[4]

[1]Department of Ultrasound, Women and Children's Hospital of Chongqing Medical University, No. 120, Longshan Road, Yubei Distinct, Chongqing 401147, China; [2]Department of Obstetrics and Gynecology, Chongqing Health Center for Women and Children, Women and Children's Hospital of Chongqing Medical University, No. 120, Longshan Road, Yubei District, Chongqing 401147, China; [3]Pediatric Research Institute, Ministry of Education Key Laboratory of Child Development and Disorders, Children's Hospital of Chongqing Medical University, Chongqing 400014, China; [4]Chongqing Key Laboratory of Ultrasound Molecular Imaging, Institute of Ultrasound Imaging, The Second Affiliated Hospital, Chongqing Medical University, No. 76, Linjiang Road, Yuzhong Distinct, Chongqing 400010, China

Received April 21, 2024; Accepted September 15, 2024; Epub October 15, 2024; Published October 30, 2024

Abstract: Ovarian cancer (OC) is a common gynecological malignant tumor with poor prognosis. One form of controlled cell death that requires iron is ferroptosis. This study utilized TCGA data analysis to identify differentially expressed genes (DEGs) related to ferroptosis in OC, revealing 2,333 up-regulated and 4,073 down-regulated genes. Venn diagrams identified 64 up-regulated and 120 down-regulated ferroptosis-related DEGs (FR-DEGs), with 15 showing a significant correlation with overall patient survival. Further analyses explored the expression, mutations, and copy number variations of these 15 FR-DEGs across various cancer types, constructing interaction networks. Molecular subtypes in OC were classified using these 15 FR-DEGs, revealing two subtypes (C1 and C2). Survival analysis identified a risk model for the C1 group based on these genes. Experimental validation highlighted TRIM46 as a key gene, with knockdown inhibiting OC cell proliferation and migration. TRIM46 was also associated with changes in ferroptosis-related markers and demonstrated a close connection with the Wnt signaling pathway, validated through Western blot experiments. Overall, the study provided a comprehensive understanding of the role of DEGs related to ferroptosis in OC, offering valuable insights into disease mechanisms and potential therapeutic targets.

Keywords: Ferroptosis, TRIM46, ovarian cancer, biomarker, metastasis, Wnt signaling pathway

Introduction

Ovarian cancer (OC) is a prevalent gynecological tumor, accounting for about 4% of all new cancer cases in women [1]. It predominantly affects postmenopausal women, particularly those over 50, though it can also occur in younger women due to genetic factors [2, 3]. The incidence of OC varies significantly by region and ethnicity. It is relatively high in western countries like Europe and North America and lower in Asian regions [4, 5]. These differences may result from genetic, environmental, and lifestyle factors. Compared to other gynecological cancers, the high mortality rate of OC is largely due to the absence of definite early symptoms and effective diagnosis methods. Traditional treatments, including debulking surgery and platinum-based chemotherapy, result in a five-year survival rate of only 47% due to chemotherapy resistance and recurrence. Hence, we urgently need to identify better biomarkers and further investigate the underlying causes of OC progression.

Ferroptosis is a unique form of cell death characterized by excessive free iron accumulation, leading to oxidative stress and lipid peroxidation, ultimately resulting in cell death [6-9]. The occurrence of ferroptosis is associated with

https://doi.org/10.62347/ONUY8904

factors such as increased cellular iron uptake, disrupted iron storage, and dysregulation of iron homeostasis. A close correlation exists with lipid peroxidation, and ferroptosis is also linked to the disruption or imbalance of the antioxidant defense system [10]. Ferroptosis has attracted widespread attention in the field of cancer biology. Some studies suggest that ferroptosis may play a role in inhibiting tumor growth and development [11, 12]. Due to the increased demands for iron in cancer cells, excessive iron can lead to oxidative stress, triggering ferroptosis. Consequently, regulating the intracellular balance of iron may have a certain impact on controlling of tumor growth [13, 14]. Although the relationship between ferroptosis and OC is not fully understood, some studies suggest that OC cells may have an increased dependency on iron, indicating that modulating of intracellular iron balance could be significant in OC treatment [15-17]. To date, the potential expression and function of ferroptosis-related genes (FRGs) in OC remain unknown to a great extent.

The purpose of this study is to identify ferroptosis-related differentially expressed genes (FR-DEGs) in OC by using TCGA data. We found that 15 FR-DEGs were significantly associated with overall survival in OC patients. Further analysis showed these genes were highly expressed in various cancers and involved in immune response, metabolism, and signaling pathways. In this study, we focused on TRIM46, demonstrating its elevated expression in OC and its crucial role in cell proliferation, migration, and ferroptosis regulation. Additionally, molecular subtypes related to the TRIM family were constructed, highlighting their potential significance in OC biology.

Materials and methods

Cell lines and cell transfection

Human OC cell lines SKOV3, A2780 and HEY were obtained from the China Center for Type Culture Collection (Wuhan, Hubei Province, China). OVCAR-3, CAOV3, SNU-8, and a control cell line IOSE80 were obtained from Wuhan Procell Corporation (Wuhan, Hubei Province, China). The cells were cultured under the following conditions: RPMI-1640 medium (Gibco, CA, USA) with 20% FBS (Gibco, CA, USA) and 1% penicillin-streptomycin solution (Excell, Taicang, Jiangsu Province, China). All cells were grown in a humidified atmosphere containing 5% CO_2 at 37°C. Moreover, the shRNAs targeting TRIM46 (shRNA-1 and shRNA-2) and the control shRNA (negative control, NC) were all synthesized and obtained from GenePharma (Suzhou, Jiangsu Province, China). Following the instructions provided by Invitrogen, we transfected shRNAs using Lipofectamine 3,000 reagent kits (Carlsbad, CA, USA). To sum up, 100 μL of Opti-MEM (Invitrogen, Carlsbad, CA, USA) was used to dilute the shRNAs at a concentration of 5 nmol/L, and 5 μL of Lipofectamine 3,000 reagent was added to mix them. Before adding the mixture to the cell culture medium, they were incubated at room temperature for 20 minutes. After 48-72 hours, the cells were either collected or utilized for further investigations.

Cell proliferation detection

Cell Counting Kit-8 (CCK-8) and 5-ethynyl-2'-deoxyuridine (EdU) incorporation assays were used to quantify the cell proliferation. To sum up, OC cells treated with TRIM46 shRNAs were seeded into a 96-well plate at a density of 2,000 cells per well for the CCK-8 experiment. Beyotime, Nantong, Jiangsu Province, China provided the CCK-8 reagents kits that were used to quantify cell proliferation after 24 hours of culture. For this purpose, 10 μL of the CCK-8 solution was added, and the optical density value at 450 nm (OD 450 nm) was determined by using a microplate reader. For EdU incorporation assays, when the cells were attached, the Click-iT EDU Alexa Fluor 488 Imaging kits (ThermoFisher, Pudong, Shanghai, China) were used for detection. In brief, the OC cancer cells were incubated with EdU (10 μM) and fixed with 4% paraformaldehyde (PFA; Sigma, Pudong, Shanghai, China), followed by treatment with Triton X-100 solution. And then, the cells were treated with 1× Apollo reaction cocktail, and the nuclei of cells were stained with DAPI solution. Finally, the fluorescence images of the cells were taken with an Olympus fluorescence microscope (Tokyo, Japan).

Transwell migration detection

The Transwell chambers (Corning, NY, USA) were used in the Transwell experiment to detect cell movement. To sum up, 600 μL of medium containing 10% FBS was added to a 12-well

plate, and 1,000 cells in 200 μL of serum-free media were placed in the upper chamber for cell migration test after 48 hours of shRNAs transfection. Cells that migrated to the lower surface of the membrane were fixed with 4% formaldehyde and stained with 0.1% crystal violet (Beyotime, Nantong, Jiangsu Province, China). Cells that did not migrate were removed from the top surface of the membrane by using cotton swabs after incubation for 24 hours at 37°C. The photos of stained cells were taken and they were quantified by using an Olympus fluorescent microscope (Tokyo, Japan) after they were washed for three times with PBS.

Real-time PCR detection

The total mRNA of OC cells after TRIM46 shRNAs treatment was purified by using RNeasy mini kits (Qiagen, Pudong, Shanghai, China) with digestion using DNase I (Thermo Scientific, Pudong, Shanghai, China). The PrimeScript® RT Reagent kits (Takara, Dalian, Liaoning Province, China) were utilized to synthesize cDNA by using 0.2 μg of RNA. For the real-time PCR experiment, the following conditions were used: PerfectStart Green qRT-PCR SuperMix Kits (TransGen Biotech, Beijing, China) 15 minutes at 95°C followed by 44 cycles of 20 seconds at 95°C, 30 seconds at 60°C, and 30 seconds at 72°C. BioRad's CFX96 Real-time PCR Detection system was used for real-time PCR. The relative expression of TRIM46 was calculated with $2^{-\Delta\Delta Ct}$ methods. GAPDH was measured as an internal control. The primers were purchased from Shenggong Biotechnology (Pudong, Shanghai, China), and the primer sequences were as follows: TRIM46: 5'-CGCCTGGTATGTCAACTC-3' (sense) and 5'-CTCCTGCTGGCATTCTTC-3' (antisense); GAPDH: 5'-CCACATCGCTCAGACACCAT-3' (sense), and 5'-ACCAGGCGCCCAATACG-3' (antisense).

Tumor growth assay in nude mice

Twelve male BALB/c nude mice (at the age of 5 weeks) were bought from Shanghai SLAC (Pudong, Shanghai, China) and randomly divided into three groups. And then, lentiviruses shRNA and sh-NC were introduced into SKOV3 cells, respectively. And then, the cells that had been treated were injected subcutaneously into the right flanks of the mice at a concentration of 1×10^7 cells/mouse. The tumors were given four weeks to grow before the mice were killed. At an interval of 4 days, Vernier calipers were used to record tumor volumes. Tumor volumes were calculated by using the formula: Volumes (mm^3) = length × $width^2$ ×0.5. Animal studies were approved by the Ethics Committee of Women and Children's Hospital of Chongqing Medical University.

Protein collection and western blot analysis

Following treatment with TRIM46 shRNAs, SKOV3 and OVCAR-3 cells were lysed in newly made RIPA buffer that contained 1× M PMSF (Sigma, Pudong, Shanghai, China) and 1× protease inhibitor cocktail (Roche, Pudong, Shanghai, China). It was centrifugated at 12,000 rpm for 10 minutes at 4°C to clean the protein lysates. We used BCA assay kits (Thermo Scientific, Pudong, Shanghai, China) to measure the protein concentration after collection of the supernatants. Subsequently, 8-12% SDS-PAGE was applied to the same protein samples. Millipore PVDF membranes (Darmstadt, Germany) were used for electro-transferring the isolated proteins. After the membranes were soaked in TBST with 5% BSA for 1 hour at room temperature, non-specific binding could no longer occur. After that, the membranes were treated with the corresponding primary antibodies against TRIM46, cyclin D1, c-Myc, and GAPDH. The incubation process was implemented overnight at 4°C. The antibodies were purchased from ProteinTech, Wuhan, Hubei Province, China, and Abcam, Pudong, Shanghai, China, respectively. The membranes were treated with the appropriate secondary antibodies the following day after three times of TBST washing. The immuno-reactive proteins were observed by using an enhanced chemiluminescence (ECL) reagent kit from Thermo Scientific in Pudong, Shanghai, China.

Measurement of malondialdehyde (MDA) levels

To assess the relative concentration of MDA, lipid peroxidation kits (#ab118970; Abcam, Pudong, Shanghai, China) were utilized. Briefly, TRIM46 shRNAs were transfected into SKOV3 or OVCAR-3 cells in 6-well plates. After 48 hours, cells were rinsed with PBS, and 300 μL of MDA lysis buffer was added, followed by centrifugation (12,000× g, 5-10 min). The resulting supernatants were collected, and a mixture of 20 μL of supernatants and 60 μL of

thiobarbituric acid (TBA) solution was prepared in a 96-well plate. Such mixture was then incubated at 95°C for 50 minutes. Subsequently, the absorbance at a wavelength of 532 nm was measured by using a BioTek microplate reader (Winooski, VT, USA).

Examination of ferrous iron (Fe^{2+}) levels

The ferrous iron (Fe^{2+}) levels in each experimental group were determined by using Abcam iron assay kits (#ab83366; Pudong, Shanghai, China). In brief, SKOV3 or OVCAR-3 cells after shRNA transfection were harvested and rinsed with icy PBS. Subsequently, 5× volumes of iron assay buffer were added to the cells, followed by centrifugation (12,000× g, 5-10 min), and the resulting supernatants were collected. The next step was to add the iron reducer to the supernatants. And then, let the mixture stand at room temperature for half an hour. After this, 10 μL of iron probe was added to every sample and left to incubate at room temperature for an additional half an hour. Then, a BioTek microplate reader (Winooski, VT, USA) was used to measure the absorbance at a wavelength of 593 nm.

Detection of glutathione (GSH) and glutathione disulfide (GSSG)

For the assessment of the relative concentration of GSH in each experimental group, glutathione (GSH) assay kits (CS0260; Sigma, Pudong, Shanghai, China) were used, while kits from Cayman (#703002; Ann Arbor, Michigan, USA) were used to determining the relative concentration of GSSG. In brief, SKOV3 or OVCAR-3 cells were collected and washed with icy PBS following TRIM46 shRNA transfection. Subsequently, lysis buffer (Beyotime, Haimen, Jiangsu Province, China) supplemented with a protease inhibitor cocktail (Roche, Pudong, Shanghai, China) was used for cell lysis. Following centrifugation (12,000× g, 5-10 min), the resulting supernatants were collected.

The GSH detection involved the addition of 50 μL of the GSH assay mixture from the kits into each sample, followed by incubation for 50 minutes at room temperature. The absorbance at a wavelength of 412 nm was then measured by using a BioTek microplate reader (Winooski, VT, USA). Similarly, for GSSG detection, the procedures were implemented with the GSSG assay kits. Initially, the supernatants were treated with 2-vinylpyridine (#13229-2; Sigma, Pudong, Shanghai, China) to eliminate GSH. Subsequently, the suspensions were incubated for 50 minutes to block the thiol group of the pre-existing GSH. The reduction of GSSG was achieved by adding 95 μL of NADPH (2 mg/ml) and 5 μL of glutathione reductase (2 units/ml). The resulting samples (50 μL) were then added to a 96-well plate, along with the addition of 150 μL of the GSSG assay cocktail mixture. Following incubation in the dark for 30 minutes, the absorbance at 412 nm was measured by using a BioTek microplate reader (Winooski, VT, USA).

Data collection and identification of differentially expressed genes (DEGs)

The Cancer Genome Atlas (TCGA) database (https://portal.gdc.cancer.gov/) was used to obtain gene expression data and clinical information from both tumor and normal tissues in OC. 564 ferroptosis-related genes (FRGs) were obtained from the FerrDb database (http://www.zhounan.org/ferrdb/current/). The Kaplan-Meier plotter database (http://kmplot.com/analysis/index.php?p=background) provided genes significantly associated with overall survival in OC based on TCGA data. Additionally, mRNA expression matrix of the cell line of tumors was obtained from the CCLE dataset (https://portals.broadinstitute.org/ccle). The differentially expressed genes (DEGs) in OC were identified by using TCGA data through the "limma" package in R software. The threshold was set as P value < 0.05 and |log2(FC)| > 1. The Venny2.1 tool (https://bioinfogp.cnb.csic.es/tools/venny/) was used to identify overlapping DEGs among TCGA-DEGs and FRGs. The heatmap and volcano map in this study were generated by using the R package "ggplot".

Prognostic signature model construction, identification of molecular subtypes and gene function analysis

In addition, the prognostic signature models were built by using the "survival" and "glmnet" packages in R software, which combined two methods: "Step" analysis and multivariate cox regression analysis. The three-stage "Step" procedure began with data analysis by using multi-factor cox regression, continued with iteration by using the step function, and concluded

with the selection of the best model. We used the "ConsensusClusterPlus" package of R software to make an unsupervised consensus clustering analysis on 376 OC samples derived from TCGA datasets to identify molecular subgroups. The gene function study was done by using the R software package "clusterProfiler". The analysis included Gene Ontology (GO) and the Kyoto Encyclopedia of Genes and Genomes (KEGG). The TCGA database was used to get the gene expression data in OC, so that we could evaluate the association among genes or several genes. The heatmap depicting gene correlations was produced by using R package "ggstatsplot".

Immune-related analysis

To investigate the relationship between TRIM46 expression and diverse immune cell infiltrations across pan-cancer types, we utilized the TIMER 2.0 database (http://timer.cistrome.org/). Various immune score algorithms, including TIMER, EPIC, CIBERSORT, and XCELL, were used for this analysis. R software package "immuneeconv" was used to examine the immune networks associated with individual genes or multiple genes and their interactions with different types of immune cells. Additionally, we used the R software package "immuneeconv" to assess immune checkpoints and immune scores of distinct molecular subtypes of OC. The R software package "ggstatsplot" was used to analyze tumor mutation burden (TMB) and microsatellite instability (MSI) across pan-cancers, ensuring a comprehensive exploration of the immune landscape in our study. The web platform of Tumor Immune Dysfunction and Exclusion (TIDE) (http://tide.dfci.harvard.edu) was used to assess the response to immune checkpoint blockade (ICB) in both subtypes of cervical cancer.

Online bioinformatics analysis platforms

The gene expression, survival data (including OS and PFS), SNV, CNV, and methylation across pan-cancer types were explored by using TCGA data through the GSCA database (http://bioinfo.life.hust.edu.cn/GSCA/#/). Additionally, the GEPIA database (http://gepia.cancer-pku.cn/) was used separately for the analysis of gene expression and survival analysis. The assessment of TRIM46 expression in pan-cancers involved the use of both the TIMER 2.0 database (http://timer.cistrome.org/) and the Human Protein Atlas (HPA, https://www.proteinatlas.org/). To construct protein-protein interaction (PPI) networks for DEGs, TRIM46 and TRIM46 family members, the STRING database (https://cn.string-db.org/) was used. Besides, the identification of potential interacting proteins associated with 15 FR-DEGs involved the construction of functional protein networks by using the GeneMANIA database (http://genemania.org/search/homo-sapiens/). Furthermore, the Kaplan-Meier Plotter website (http://kmplot.com/analysis/index.php?p=service) based on TCGA data was used to generate overall survival data for genes. Additionally, we used TISIDB database (http://cis.hku.hk/TISIDB/index.php) to assess the expression of TRIM46 and tumor infiltrating lymphocytes (TILs).

Statistical analysis

Statistical analysis was made by using GraphPad Prism 7.0 and SPSS Version 16.0 software (SPSS Inc., Chicago, IL, USA). Bioinformatics data was processed by using R software (Version 3.6.1, https://www.r-project.org/). All data are expressed as mean ± SEM. For comparisons between the two groups, the Student's t-test was used to assess statistical significance. For comparisons involving more than two groups, one-way ANOVA was used, followed by post-hoc tests (e.g., Tukey's or Bonferroni) to identify specific group differences. In case of multiple comparisons, the Bonferroni correction was used to adjust the significance threshold to consider Type I errors. Correlation analysis was made by using Pearson or Spearman correlation coefficients, depending on the distribution of the data. For survival analysis, the Kaplan-Meier method was used to estimate survival curves, and differences between groups were assessed by using the log-rank test. The difference was statistically significant when $P < 0.05$. All tests were two-tailed, and the exact p values were provided where applicable.

Results

Obtaining of differentially expressed genes (DEGs)

To identify ferroptosis-related DEGs (FR-DEGs) in OC, we analyzed differentially expressed genes in OC tissues by using TCGA data. We

found 2,333 up-regulated genes and 4,073 down-regulated genes in OC compared to normal tissues. Volcano plots and heatmaps of these DEGs are shown in **Figure 1A** and **1B**. KEGG pathway analysis of these genes is presented in **Figure 1C**. By using Venn diagrams, we identified 64 up-regulated FR-DEGs and 120 down-regulated FR-DEGs in OC (**Figure 1D**). KEGG analysis of these FR-DEGs is shown in **Figure 1E** and **1F**. Kaplan-Meier survival analysis revealed 15 FR-DEGs were significantly correlated with overall survival in OC (**Figure 1G**).

The expression and genetic changes analysis of 15 FR-DEGs in pan-cancers

Next, we tried to analyze the expression of the 15 FR-DEGs in numerous types of cancer, and the data suggested that many of them were highly expressed in most types of cancer, including TRIM46, CDC25A, CDKN2A, AURKA, CDCA3, and KIF20A (**Figure 2A**). Moreover, the overall survival (OS) of different cancers was also analyzed by using GSCA database, and the result indicated that most of these 15 FR-DEGs were significantly related with OS in LGG, KIRC, ACC, KICK and KIRP (**Figure 2B**). Afterwards, the mutation profiles of the 15 FR-DEGs were evaluated by using GSCA database, and the result indicated that the top 10 mutated genes in cancers were CDKN2A, NRAS, TRIM46, MMP13, KIF20A, CCDC6, CDC25A, GPT2, PRDX6, and CAPG (**Figure 2C**). The copy number variation (CNV) of the 15 FR-DEGs across cancer types was then also investigated. The data using CNV pie distribution revealed that CEBPG, CDCA3, PRDX6, TRIM46, and AURKA were heterozygous copy number amplifications in most cancers (**Figure 2D**). In addition, the correlation analysis demonstrated that the mRNA expression levels of the most 15 FR-DEGs were positively correlated with their copy number levels in most cancers, especially in KIRC, READ, LIHC, GBM, TGCT, LGG, UCEC, STAD, PAAD, COAD, SARC, LUAD, UCS, SKCM, BRCA, BLCA, LUSC, ESCA, OC, CESC, and HNSC (**Figure 2E**).

The methylation, gene-pathway and gene-interaction networks analysis of 15 FR-DEGs

We investigated the methylation of the 15 FR-DEGs across various cancers. MMP13, CEBPG, CDCA3, and NQO1 had low methylation in several types of cancer, including BLCA, PAAD, UCEC, LUSC, LIHC, BRCA, HNSC, LUAD, and ESCA (**Figure 3A**). Methylation levels of these FR-DEGs were generally negatively correlated with their mRNA expression in most cancers (**Figure 3B**). Survival analysis indicated that methylation differences of the 15 FR-DEGs did not significantly affect survival in most cancers, except LGG and KIRC (**Figure 3C**). We also explored the interactions of the 15 FR-DEGs with key pathways, as shown in **Figure 3D**, and constructed a protein-protein interaction network for these genes by using the STRING database (**Figure 4A**) and individual networks by using GeneMANIA (**Figure 4B-P**).

Identification of 15 FR-DEGs-related molecular subtypes in OC

Tumor heterogeneity is very important in tumorigenesis, metastasis, development and progression. Therefore, next, our purpose is to identify the molecular subtypes in OC by using 15 FR-DEGs identified above. To achieve this objective, we made an unsupervised consensus clustering analysis of 376 OC samples based on TCGA datasets by using the R software "ConsensusClusterPlus" package. After analysis, the consensus cumulative distribution function (CDF) plot (**Figure 5A**), the delta area (**Figure 5B**), and the consensus matrix were obtained (**Figure 5C**). The data suggested that 376 OC samples could be divided into two molecular subtypes including Group C1 (Group 1; 221 HCC samples) and Group C2 (Group 2; 155 HCC samples). The differentially expressed genes of the two groups (Group 1 vs. Group 2) were further identified, and the volcano plot was shown in **Figure 5D**. In addition, the overall survival (OS) and progression-free survival (PFS) of the OC patients in the two molecular subtypes were analyzed though there was no significant difference in both groups (**Figure 5E** and **5F**). Besides, the DEGs of the two groups were further used for the GO and KEGG pathway analysis. The GO analysis revealed that these DEGs were related with regulation of chromosome separation, regulation of mitotic metaphase/anaphase transition, regulation of mitotic nuclear division, regulation of mitotic sister chromatid segregation, and spindle organization (**Figure 5G**). The KEGG analysis suggested that the DEGs were related with Oocyte meiosis, platinum drug resistance, progesterone-mediated oocyte maturation, pyrimidine metabolism, ubiquitin-mediated proteolysis, viral carcinogenesis, and p53 signaling pathway (**Figure 5H**).

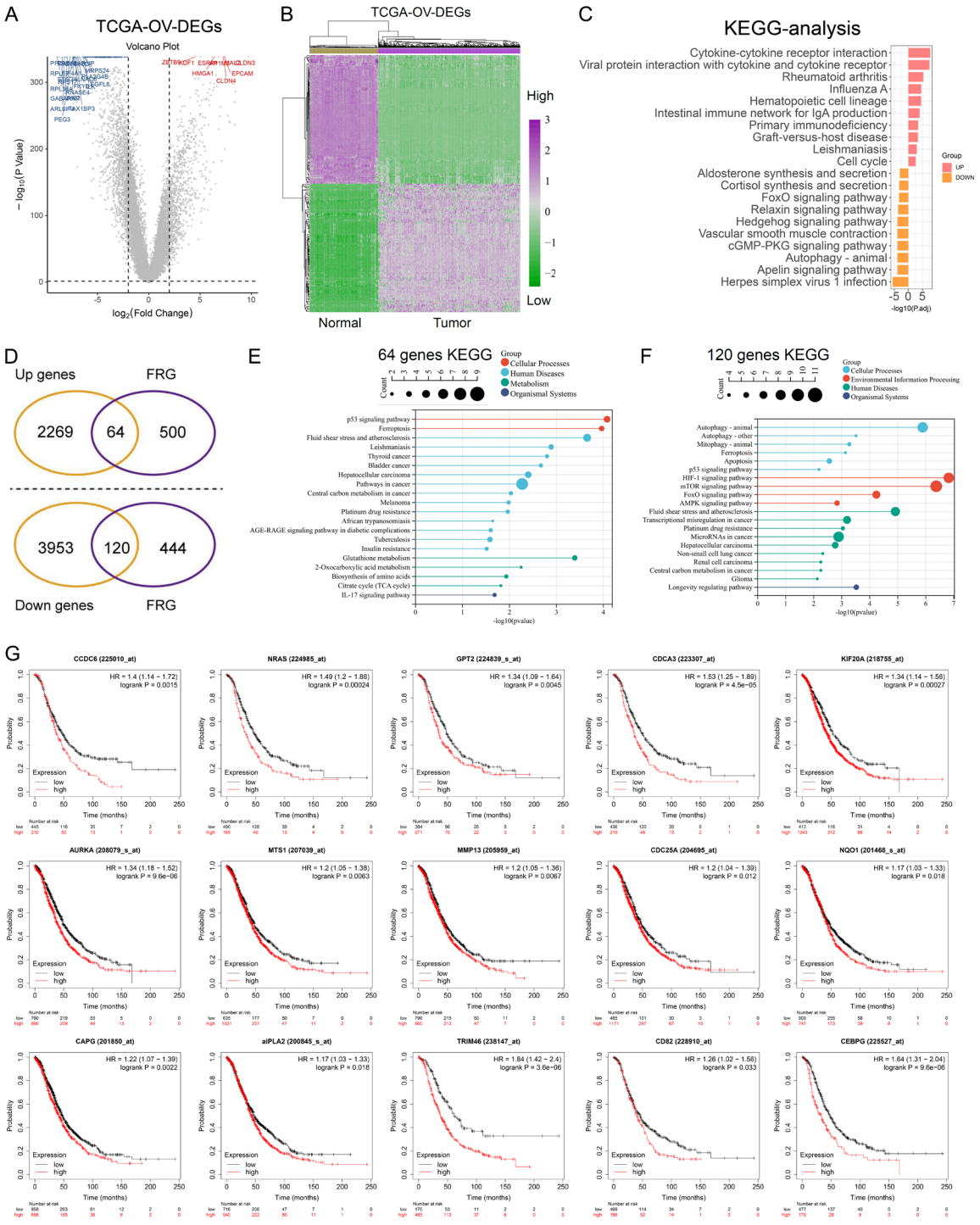

Figure 1. Differential expression analysis of OC tissues based on TCGA data. A. Volcano plot illustrating 2333 up-regulated genes (red dots) and 4,073 down-regulated genes (blue dots) in OC tissues compared to normal tissues. B. Heatmap representation of the differentially expressed genes (DEGs) in OC tissues. C. KEGG pathway analysis of both up- and down-regulated genes in OC. D. Venn diagrams depicting the identification of ferroptosis-related DEGs (FR-DEGs) in OC, revealing 64 up-regulated FR-DEGs and 120 down-regulated FR-DEGs. E. KEGG pathway analysis specifically for the 64 up-regulated FR-DEGs. F. KEGG pathway analysis dedicated to the 120 down-regulated FR-DEGs. G. Kaplan-Meier plotter analysis of the overall survival (OS) for the 64 up-regulated FR-DEGs, highlighting 15 genes (15 FR-DEGs) significantly correlated with OS in OC based on TCGA data.

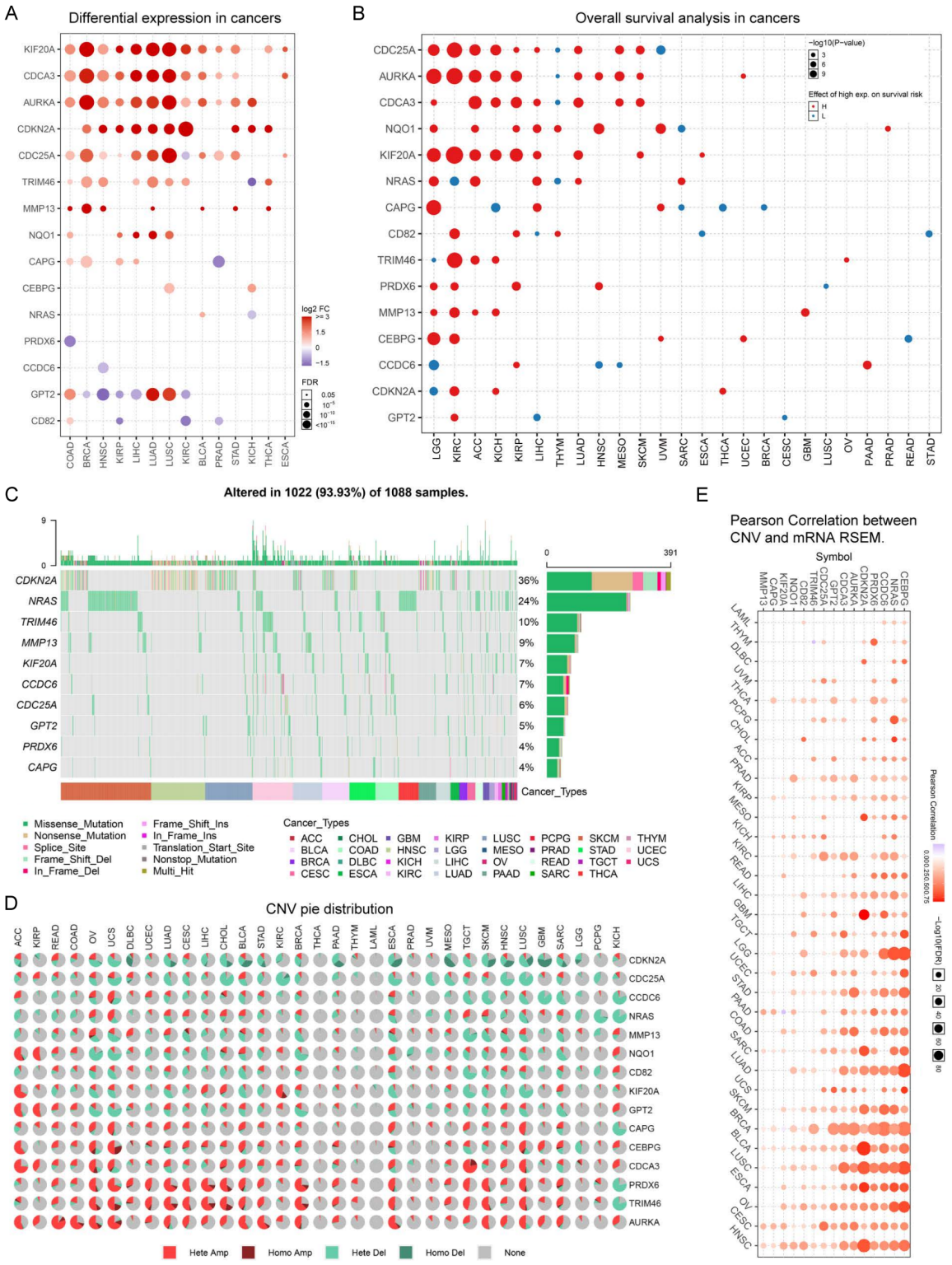

Figure 2. Expression and genetic changes analyses of 15 FR-DEGs across pan-cancers. A. Expression analysis of 15 FR-DEGs in various cancer types. B. Overall survival (OS) analysis of 15 FR-DEGs in different cancers. C. Mutation profiles of 15 FR-DEGs in cancers. D. Copy number variation (CNV) of 15 FR-DEGs across cancer types. E. Correlation analysis between mRNA expression and copy number levels of 15 FR-DEGs.

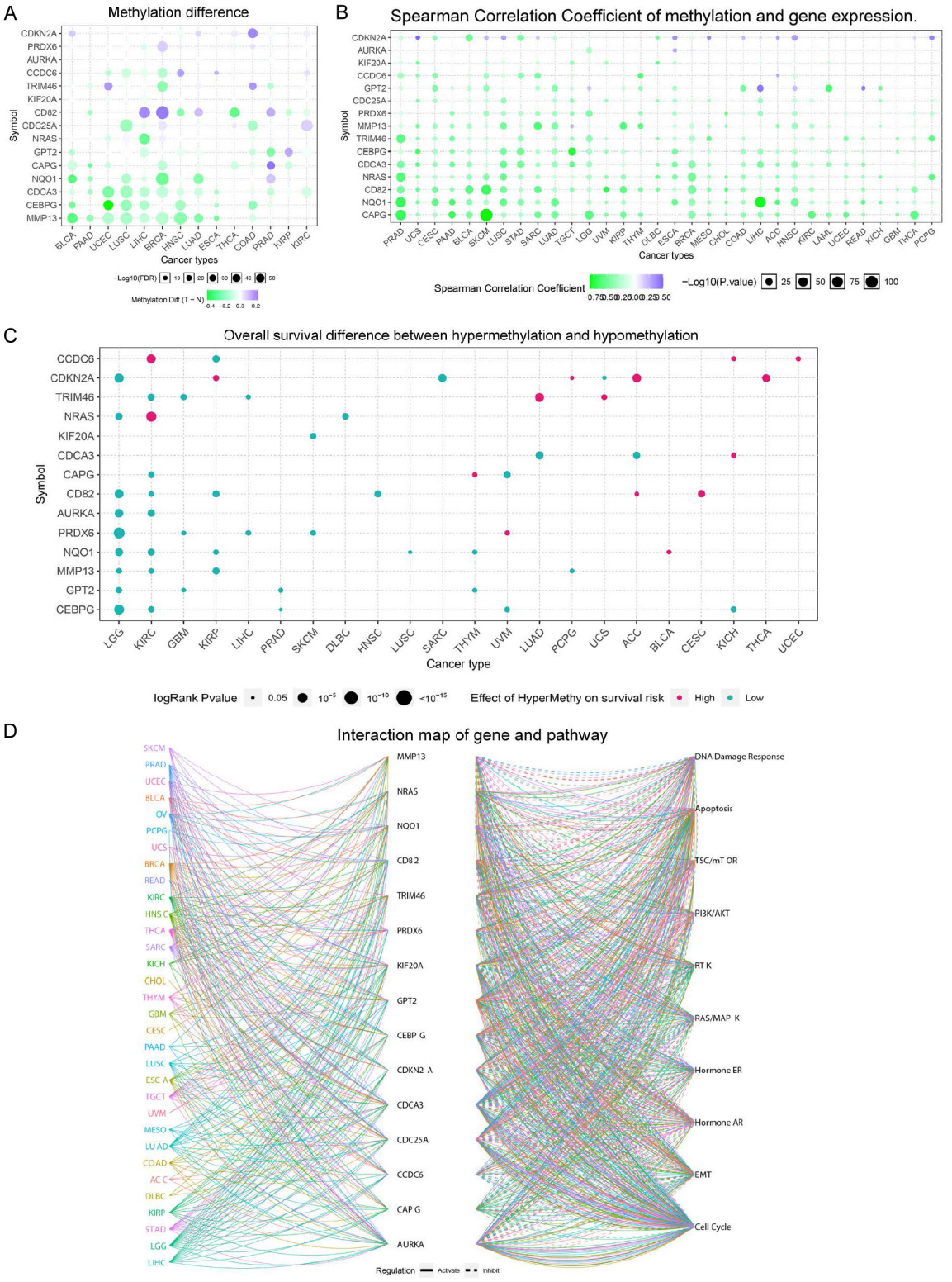

Figure 3. Methylation, gene-pathway, and gene-interaction networks analyses of 15 ferroptosis-related differentially expressed genes (FR-DEGs). A. Methylation analysis of 15 FR-DEGs in pan-cancers. B. Correlation between methylation and mRNA expression of 15 FR-DEGs. C. Overall survival difference based on methylation levels of 15 FR-DEGs across cancers. D. Gene-pathway and gene-interaction networks.

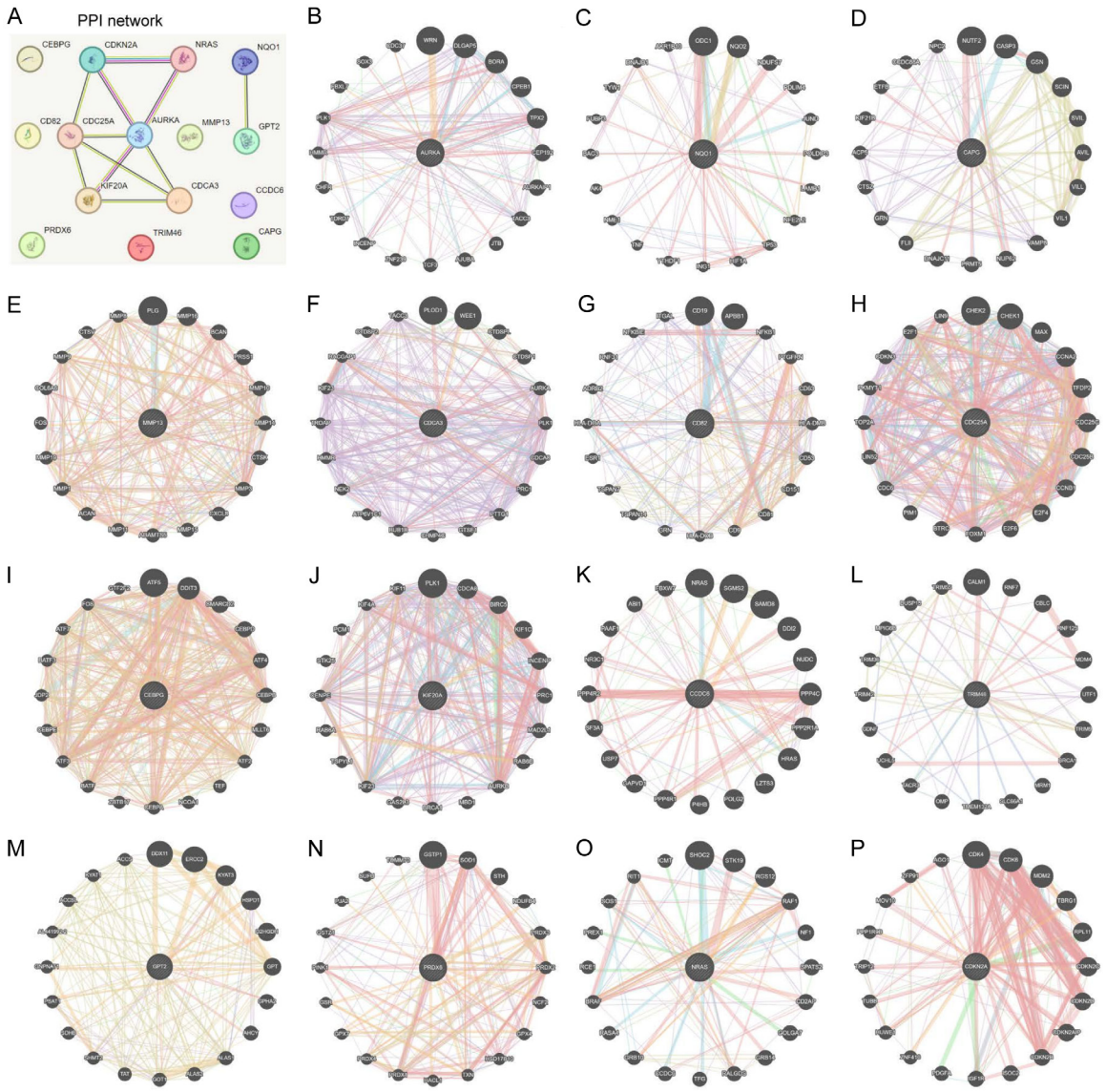

Figure 4. Protein-protein interaction networks of 15 FR-DEGs. A. Protein-protein interaction network of all 15 FR-DEGs. B-P. Individual protein-protein interaction networks for each FR-DEG. Separate construction of protein-protein interaction networks for each of the 15 FR-DEGs using the GeneMANIA database.

Construction of the prognostic model of 15 FR-DEGs of the two molecular subtypes in OC

Our above analysis indicated that the 15 FR-DEGs were closely relevant with OC, and had divided the OC samples into two molecular subtypes. Therefore, we next sought to utilize two methods including "Step" analysis and multivariate cox regression analysis to respectively predict prognostic models for the two molecular subtypes in OC. The three-stage "Step" procedure began with data analysis using multifactor cox regression, continued with iteration using the step function, and concluded with the selection of the best model. The "Step" method was used for predicting the prognostic models for the two molecular subtypes (including group 1 and group 2), respectively. The results suggested that there was no appropriate prognostic model of group 2 (including 150 OC samples), while the optimal model was predicted in group 1 (including 221 OC samples), and the formula used for risk score computation was as follows: riskscore = (0.1927) * CAPG + (-0.1277) * CDKN2A + (-0.3328) * PRDX6 + (-0.2315) * GPT2 + (0.3808) * CEBPG + (0.2743) * CDCA3. Based on the median threshold obtained by the risk score model,

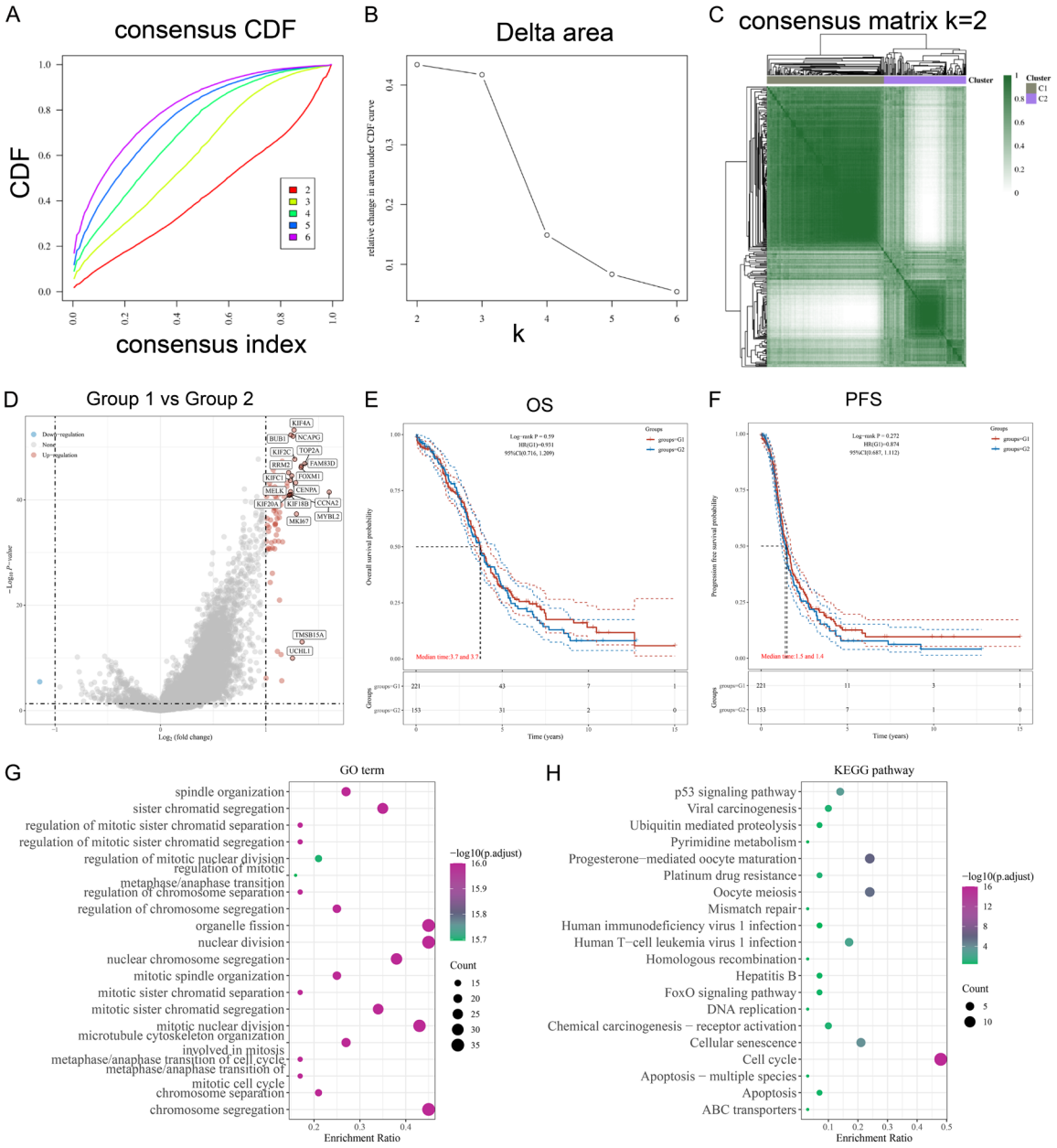

Figure 5. Identification of molecular subtypes and analysis of differentially expressed genes (DEGs) in OC based on 15 ferroptosis-related differentially expressed genes (FR-DEGs). A. Consensus cumulative distribution function (CDF) Plot. Results of the unsupervised consensus clustering analysis depicting the consensus CDF plot. B. Delta area plot showing the relative change in area under the CDF curve. C. Visualization of the consensus matrix displaying the degree of agreement among OC samples in the identified molecular subtypes (C1 and C2 groups). D. Volcano plot of differentially expressed genes (DEGs). E. Kaplan-Meier plot illustrating the overall survival analysis for OC patients in the identified molecular subtypes. F. Kaplan-Meier plot displaying the progression-free survival analysis for OC patients in the identified molecular subtypes. G. Gene ontology (GO) analysis. H. Kyoto encyclopedia of genes and genomes (KEGG) pathway analysis.

221 OC patients were divided into low-risk and high-risk subgroups. Additionally, a heatmap of the 6 genes related to OC was constructed (Figure S1A). Figure S1B shows the results of the Kaplan-Meier analysis, which also demonstrated that the low-risk group had a substantially better OS than the high-risk group. In addition, using 221 OC samples and time-dependent receiver operating characteristic (ROC) analysis, we assessed the prognostic model's

effectiveness. For 1-, 3-, and 5-year OS, the area under the ROC curve (AUC) was 0.497, 0.63, and 0.663, respectively, as shown in Figure S1C. Similarly, multivariate cox regression (COX method) analysis was used to construct prognostic models using the the 15 FR-DEGs for the two molecular subtypes in OC. The results suggested that there was no appropriate prognostic model of group 1 (including 221 OC samples), while the optimal model was predicted in group 2 (including 155 OC samples), and the formula used for risk score computation was as follows: riskscore = (-0.1492) * KIF20A + (0.1909) * CAPG + (-0.0179) * CDKN2A + (-0.0874) * NRAS + (-0.0518) * PRDX6 + (-0.1469) * GPT2 + (0.0435) * TRIM46 + (-0.0174) * CCDC6 + (-0.0794) * CEBPG + (0.0666) * NQO1 + (0.0949) * AURKA + (0.0191) * CDC25A + (-0.0244) * CD82 + (-0.0729) * CDCA3 + (-0.0134) * MMP13. The heatmap of the 15 FR-DEGs in 155 OC samples was shown in Figure S1D. Beyond that, the Kaplan-Meier analysis showed that low-risk individuals had a far better OS than high-risk patients (Figure S1E). Finally, the AUC for 1-, 3-, and 5-year OS was 0.622, 0.557, and 0.705, respectively (Figure S1F).

Gene correlation analysis in the two OC molecular subtypes

Next, we sought to uncover the gene correlation in the two OC molecular subtypes. First, we analyzed the expressing correlation of the 15 FR-DEGs in group 1 and group 2, respectively, and the data suggested that most of the 15 FR-DEGs were positively correlated with each other in both OC molecular subtypes (Figure S2A and S2B). In addition, the ferroptosis-related genes expression in both OC molecular subtypes (group 1 and group 2) was analyzed and presented using heatmap. The data indicated that most of the ferroptosis-related genes expressed significantly differentially in group 1 and group 2 (Figure S2C). Then, the ferroptosis-related gene correlation in group 1 and group 2 was analyzed (Figure S2D and S2E). Similarly, the m6A-related genes expression and correlation were also analyzed in both OC molecular subtypes (Figure S2F-H).

The immune-related analyses in the two molecular subtypes of OC

We evaluated immune scores, including Macrophage, Tregs, B cells, NK cells, CD4+ T cells, CD8+ T cells, and Neutrophils, in the two OC molecular subtypes using the CIBERSORT method. Significant differences were observed in Monocyte, Macrophage M1, and Neutrophil scores between the two groups (Figure S3A). Additionally, the expression of immune checkpoints CD274, HAVCR2, and PDCD1LG2 varied significantly between the subtypes (Figure S3B). Although the immune checkpoint blockade (ICB) response did not differ significantly between the groups (Figure S3C), immune interaction networks involving 15 FR-DEGs and various immune cells were constructed for each subtype (Figure S3D and S3E).

The expression and survival analyses of TRIM46 in pan-cancers

Based on our analysis indicating potential relevance of the 15 FR-DEGs in OC, we focused on TRIM46, a candidate regulator of tumorigenesis, for further investigation. We first examined TRIM46 expression in OC samples using TCGA data and found it significantly higher compared to normal tissues (Figure S4A). We also analyzed TRIM46 expression across different OC stages and grades (Figure S4B and S4C), and assessed overall survival of patients with high and low TRIM46 expression using the Kaplan-Meier plotter database (Figure S4D). Additionally, TRIM46 expression was evaluated across various cancer types using the TIMER database (Figure S4E) and within different OC tissue cells using the TISCH2 database, revealing high expression in OC cells and fibroblasts (Figure S4F). Finally, we explored TRIM46's impact on overall survival in pan-cancers using TISCH2 (Figure S4G).

The immune related analyses of TRIM46 in pan-cancers

To explore the relationship between TRIM46 and cancer immunity, we first analyzed TRIM46 expression in various immune cells using the Human Protein Atlas, finding it was notably higher in Memory CD4 T-cells (Th17, Th2, and Th1/Th17) compared to other immune cells (Figure S5A). We then assessed TRIM46 expression and tumor-infiltrating lymphocytes (TILs) using the TISIDB database, revealing a positive correlation in half of the TCGA cancer types (Figure S5B). We also investigated TRIM46's correlation with chemokines, receptors,

and immunomodulators across pan-cancers (Figure S5C and S5D).

Further analysis showed that TRIM46 was positively correlated with immune checkpoint-related genes in most cancers (Figure S6A). Using the XCELL algorithm, we found TRIM46 was strongly correlated with several immune cells in OC samples, including naive B cells, eosinophils, mast cells, and various T cell subsets (Figure S6B). Additionally, we examined the correlation between TRIM46 and tumor mutation burden (TMB) and microsatellite instability (MSI) across cancers, finding significant correlations in over half of the TCGA cancer types (Figure S6C and S6D).

The immune analyses in TRIM46 high and low groups

To investigate the role of TRIM46 in cancer immunity, we categorized OC samples into TRIM46 high and low groups and compared their immune profiles. Analysis using the CIBERSORT algorithm revealed significant differences in several immune cell types between the groups, including T cell CD4+ central memory, Mast cells, T cell CD4+ Th1, Th2, CD8+ naive, and others (Figure S7A). The distribution of 22 immune cell types in each group is shown in Figure S7B, highlighting immune cell heterogeneity. We also assessed immune checkpoint expression, noting a significant difference in TIGIT between the groups (Figure S7C). The immune checkpoint blockade (ICB) response was significantly different between TRIM46 high and low groups (Figure S7D). Lastly, immune interaction networks for TRIM46 and various immune cells were constructed for both groups (Figure S7E and S7F).

Differentially expressed genes, GO and KEGG analyses in TRIM46 high and TRIM46 low group

Next, we further obtained the differentially expressed genes (DEGs) in TRIM46 low and TRIM46 high group, and there were 25 up-regulated genes (TRIM46 low group vs. TRIM46 high group) and 316 down-regulated genes. The volcano plot and heatmap were respectively presented in Figure S8A and S8B. After that, the gene ontology (GO) related GSEA analysis using R software package "clusterProfiler" and "enrichplot", including the biological process (BP), cellular component (CC) and molecular function (MF) categories, were also carried out and displayed in Figure S8C-E, respectively. Moreover, the KEGG analysis revealed that these DEGs were correlated with Human papillomavirus infection, Wnt signaling pathway, Axon guidance, Focal adhesion, ECM-receptor interaction and Hippo signaling pathway (Figure S8F). In addition, we extracted the top 20 signaling pathways from the above KEGG analysis, and the data suggested that these DEGs were closely correlated with PI3K-Akt signaling pathway, Wnt signaling pathway, Hippo signaling pathway, MAPK signaling pathway, Rap1 signaling pathway and Ras signaling pathway (Figure S8G).

The correlation of TRIM46 and metabolism pathways

Since the emerging reports had revealed that the metabolism was a crucial factor to modulate tumor development and progression, we thus sought to investigate the correlation between the TRIM46 and several metabolism pathways. According to the data, TRIM46 was significantly positively correlated with Inositol_phosphate_metabolism (Figure S9A), Valine_leucine_and_isoleucine_biosynthesis (Figure S9B), TGFB (Figure S9C), Neomycin_kanamycin_and_gentamicin_biosynthesis (Figure S9D), and Lysine_degradation (Figure S9E). Besides, TRIM46 was markedly negatively correlated with Pyruvate_metabolism (Figure S9F), Lipoic_acid_metabolism (Figure S9G), DNA_repair (Figure S9H), and Apoptosis (Figure S9I).

The expression, survival, molecular subtype classification and PPI network of TRIM family in pan-cancers

The TRIM family comprises roughly 70 proteins characterized by a coiled-coil domain, an N-terminal RING finger, and one or two B-boxes. Previous studies have linked TRIM proteins to tumor development. We investigated the expression of TRIM family members in pan-cancers and found that nearly half, including TRIM32, TRIM38, TRIM46, and others, were highly expressed in various cancer types, while others showed low or absent expression (Figure S10A). Survival analysis revealed significant correlations between most TRIM members and overall survival across different cancers (Figure S10B). We used unsupervised consensus clustering of

376 OC samples to identify molecular subtypes, revealing three distinct subtypes (Figure S10C). Additionally, we constructed a PPI network for TRIM family members using the STRING database (Figure S10D).

TRIM46 knockdown inhibited the proliferation and migration of OC cells

To investigate TRIM46's role in OC, we analyzed its expression in various cancer cell lines using the CCLE database, finding high levels in OC cell lines like Caov-4 and OVCAR-3 (**Figure 6A** and **6B**). We confirmed high TRIM46 expression in SKOV3 and OVCAR-3 via qRT-PCR and western blot (**Figure 6C**) and used these lines for further experiments. We synthesized shRNAs targeting TRIM46, achieving over 70% knockdown efficiency (**Figure 7A** and **7B**). CCK-8 assays showed that TRIM46 knockdown significantly reduced cell proliferation in SKOV3 and OVCAR-3 (**Figure 7C** and **7D**). EdU assays further confirmed reduced cell growth (**Figure 7E** and **7F**), while transwell assays indicated decreased cell migration (**Figure 7G**). In vivo, TRIM46 knockdown resulted in significantly smaller tumors compared to controls (**Figure 7H**).

The suppression of TRIM46 induces ferroptosis of OC cells and affects Wnt signaling

To evaluate TRIM46's impact on ferroptosis, we first analyzed its correlation with ferroptosis driver genes using TCGA data, finding a significant positive correlation (**Figure 8A**). We then assessed ferroptosis-related indices in OC cells after TRIM46 knockdown. Results showed increased malondialdehyde (MDA) and Fe^{2+} levels, alongside decreased GSH and increased GSSG (**Figure 8B-E**), indicating enhanced ferroptosis. Additionally, western blot analysis revealed reduced β-Catenin, cyclin D1, and c-Myc levels in SKOV3 and OVCAR-3 cells, suggesting that TRIM46 depletion affects Wnt signaling (**Figure 9A** and **9B**).

Discussion

The clinical prognosis of OC is relatively complex, primarily due to the lack of typical symptoms in the early stages, leading to most patients being diagnosed at advanced stages [18, 19]. Late-stage OC has a poorer prognosis due to its tendency to spread to other regions of the pelvic and abdominal cavities. Early detection is critical for improving the survival rates of OC patients. However, the lack of specific symptoms and effective screening tools makes early-stage diagnosis particularly challenging [20, 21]. In the screening, diagnosis, and prognosis assessment of ovarian cancer (OC), commonly used tumor markers include CA-125, HE4, CA19-9, and CEA. While CA-125 is sensitive in detecting late-stage OC and recurrence, its lack of specificity and the possibility of normal levels in early-stage patients limit its effectiveness for early detection [22-24]. HE4 exhibits higher sensitivity and specificity in detecting early-stage ovarian cancer (OC), though its levels may be affected by other gynecological conditions. CA19-9 shows some sensitivity in late-stage OC but lacks specificity, while CEA, a general tumor marker, has limited specificity, particularly in early OC diagnosis. In summary, although these tumor markers contribute to the clinical management of OC, their individual use remains constrained by significant limitations.

Ferroptosis is a specific form of iron-dependent cell death distinguished from other cell death pathways such as apoptosis and necrosis [25]. A key feature of ferroptosis is the accumulation of lipid peroxides, which causes damage to the cell membrane. In OC, studies indicate that ferroptosis may play a role in both the disease's pathogenesis and its response to treatment [26-28]. On the one hand, ferroptosis in OC cells might be involved in the tumor's antioxidant defense. Certain OC cells may manipulate iron metabolism pathways to increase iron accumulation, thereby promoting cell survival and proliferation. The regulation of ferroptosis could play a crucial role in OC cells, influencing their ability to cope with oxidative stress [29, 30]. On the other hand, ferroptosis could offer new therapeutic strategies for OC treatment. Some research indicates that by modulating ferroptotic pathways, it is possible to induce the death of OC cells, thereby enhancing treatment effectiveness [31, 32]. Drugs targeting iron metabolism and ferroptosis present promising therapeutic avenues for OC treatment. This study identified ferroptosis-related differentially expressed genes (FR-DEGs) in OC through an analysis of TCGA data, with fifteen FR-DEGs found to be significantly associated with overall survival. Pan-cancer analyses revealed elevated expression of key FR-DEGs

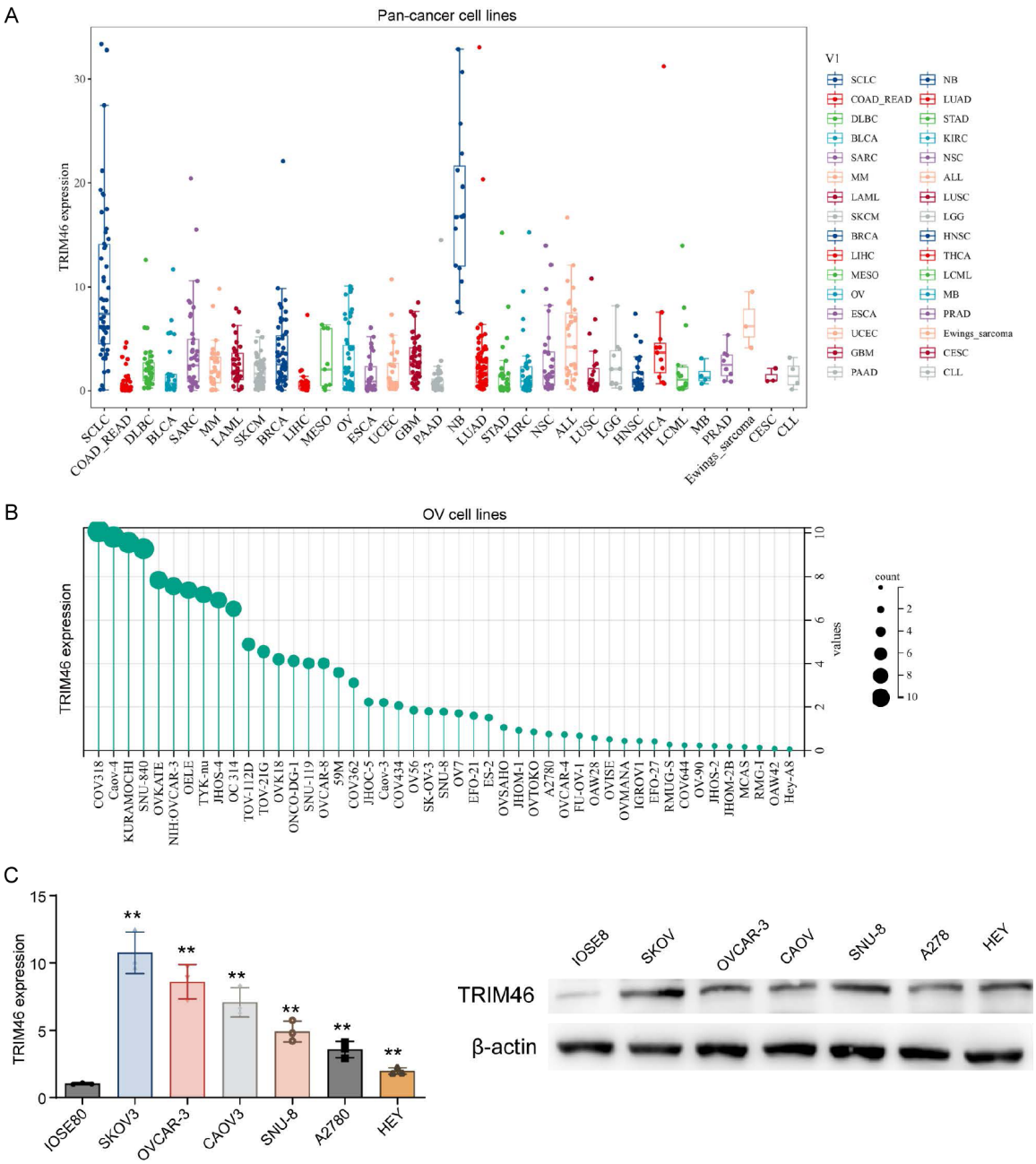

Figure 6. The expression pattern of TRIM46 in various cancer cell lines. A. Exploration of TRIM46 expression in different cancer cell lines across various cancer types using the CCLE database. B. Estimation of TRIM46 expression in OC cell lines using the CCLE database, highlighting high expression in multiple OC cell lines. C. Quantitative RT-PCR and western blot validation of TRIM46 expression in selected OC cell lines (SKOV3, OVCAR-3, CAOV3, SNU-8, A2780, HEY) and a control cell line KOV3 and OVCAR-3 exhibit the highest TRIM46 expression.

across multiple cancer types. Genetic and epigenetic analyses further highlighted the roles of specific FR-DEGs, such as TRIM46 and CDKN2A. The study also uncovered two molecular subtypes in OC and developed prognostic models based on FR-DEGs, offering valuable insights for personalized treatment strategies. These findings enhance our understanding of ferroptosis-related gene expression and its clinical significance in OC.

Then, we delved into gene correlations, m6A-related gene expression, and immune-related analyses in two molecular subtypes of OC. In

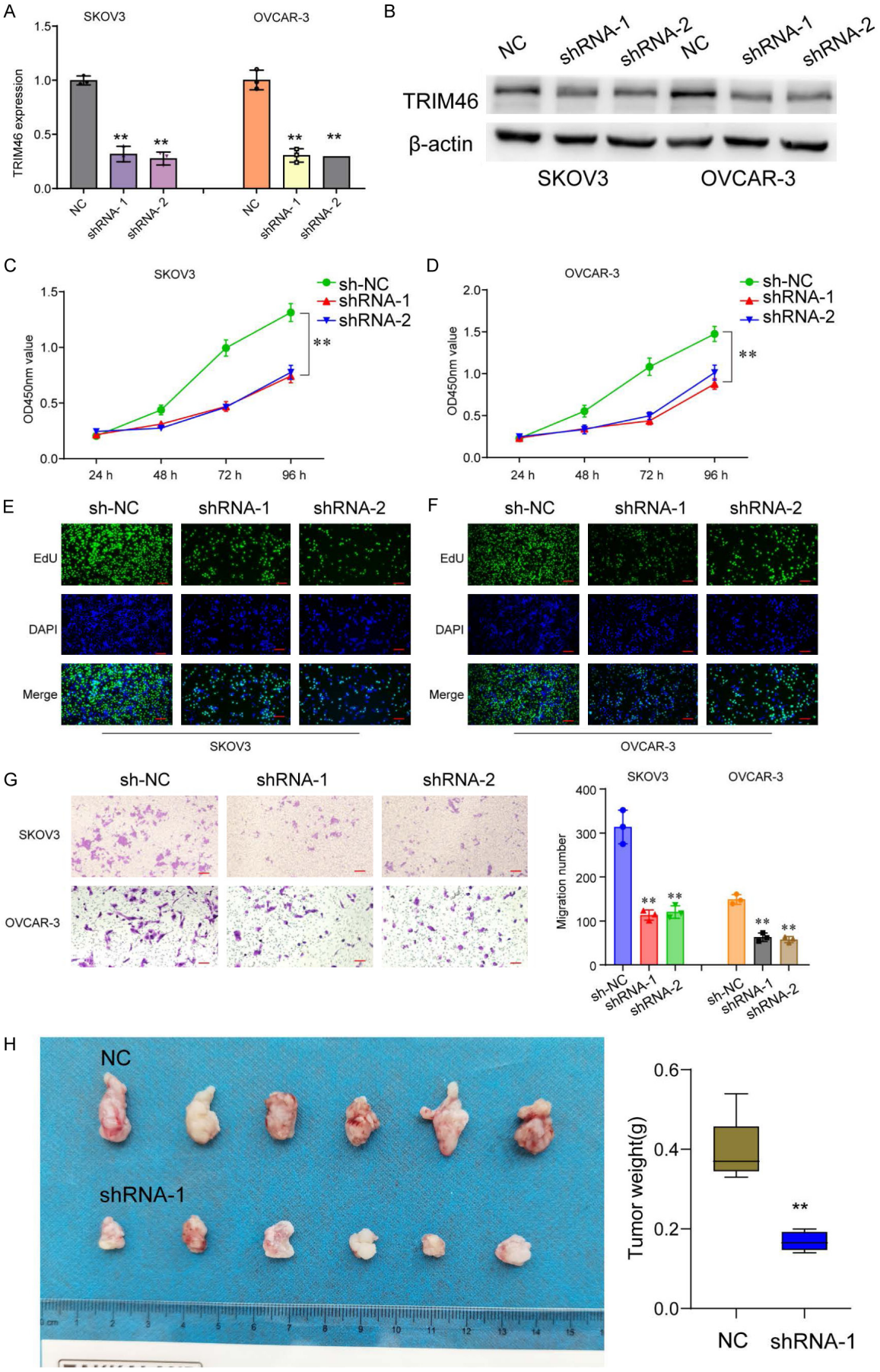
A
SKOV3
OVCAR-3
TRIM46 expression
NC
shRNA-1
shRNA-2
B
NC
shRNA-1
shRNA-2
TRIM46
β-actin
SKOV3
OVCAR-3
C
SKOV3
sh-NC
shRNA-1
shRNA-2
OD450nm value
24 h
48 h
72 h
96 h
D
OVCAR-3
E
sh-NC
shRNA-1
shRNA-2
EdU
DAPI
Merge
F
G
Migration number
H
Tumor weight(g)

Figure 7. TRIM46 knockdown inhibits OC cell proliferation. A, B. Assessment of TRIM46 knockdown efficiency using qRT-PCR and western blot assays after transfection with TRIM46-targeting shRNAs in SKOV3 and OVCAR-3 cells. C, D. CCK-8 assays revealing the inhibitory effect of TRIM46 knockdown on the proliferation of SKOV3 and OVCAR-3 cells. E, F. EdU incorporation assays showing the reduction in proliferating cells following TRIM46 knockdown in SKOV3 and OVCAR-3 cells. Scale bars: 20 μm. G. Transwell migration assays demonstrating the inhibitory effect of TRIM46 knockdown on the migration of both SKOV3 and OVCAR-3 cells. Scale bars: 100 μm. H. The image of xenografts isolated from mice one month and the tumor weights.

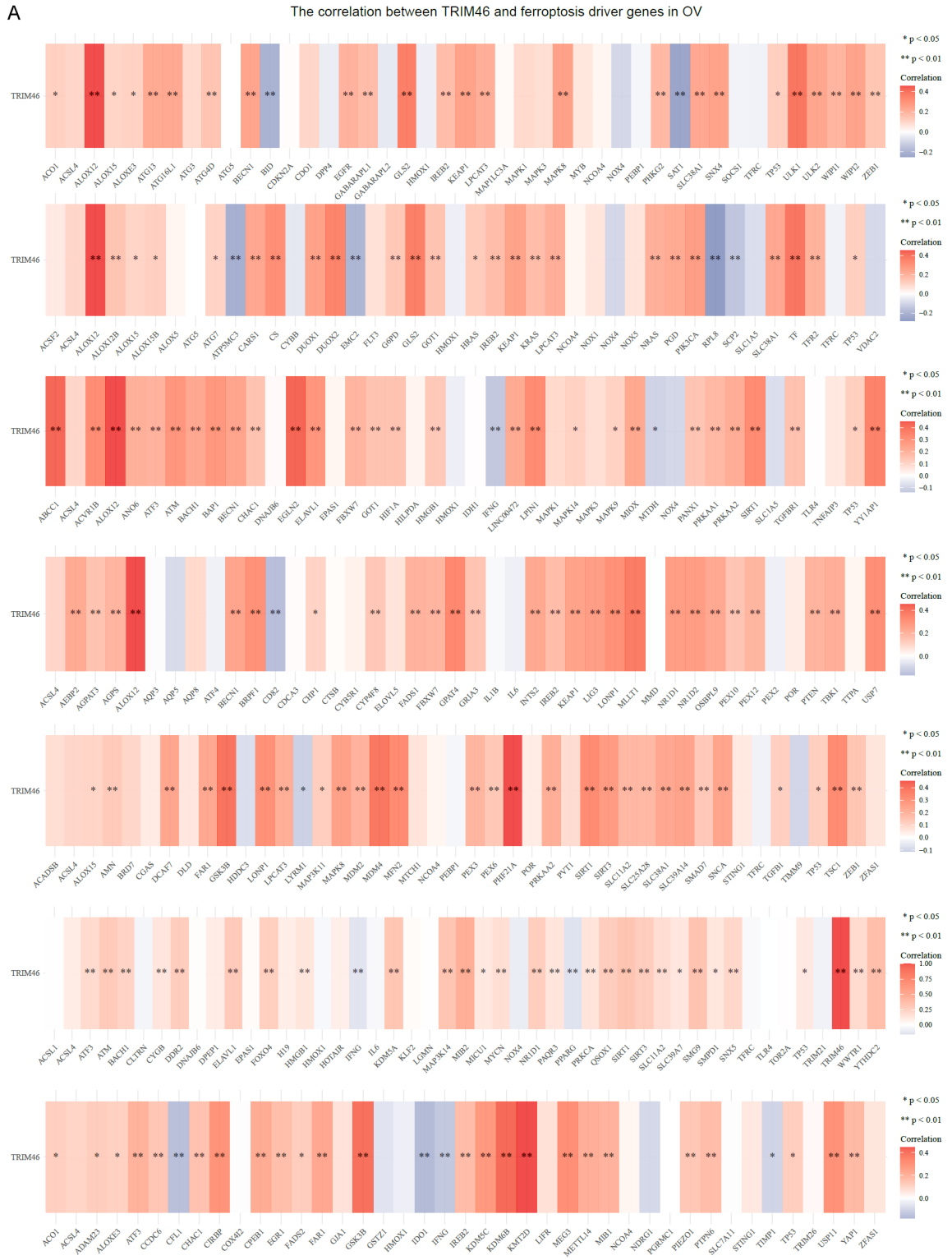

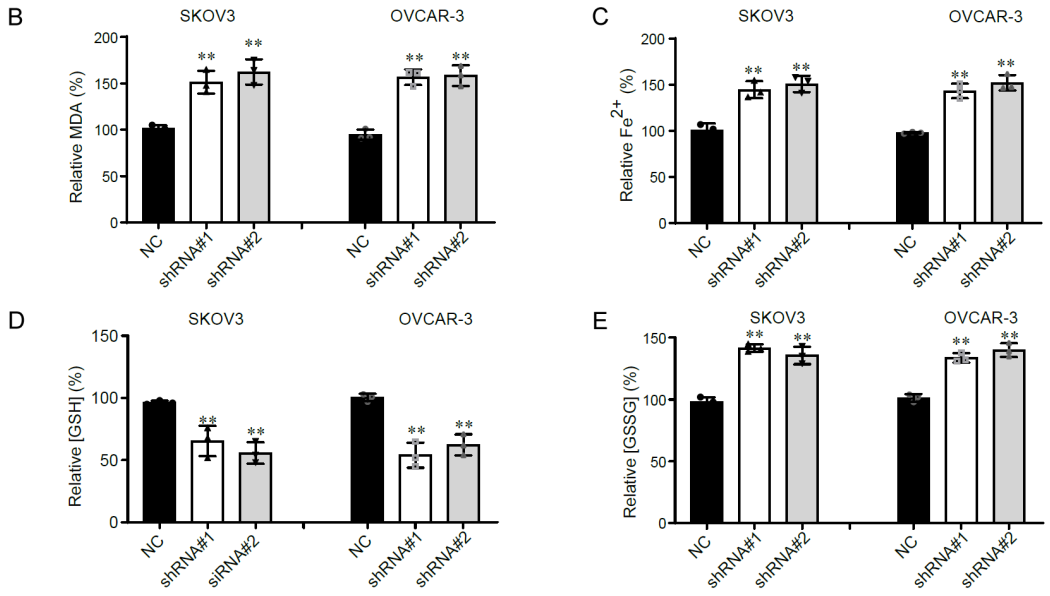

Figure 8. The suppression of TRIM46 induces ferroptosis of OC cells. A. Bioinformatic analysis depicting the significant positive correlation between TRIM46 and various ferroptosis driver genes in OC samples based on TCGA dataset. B. Assessment of malondialdehyde (MDA) levels in OC cells after TRIM46 depletion, indicating a notable increase in relative MDA levels. C. Determination of relative Fe^{2+} levels in OC cells upon TRIM46 depletion, revealing a marked elevation. D. Evaluation of relative GSH levels in OC cells following TRIM46 depletion, demonstrating a significant decrease. E. Assessment of relative GSSG levels in OC cells after TRIM46 depletion, showing a substantial increase.

both subtypes, the 15 FR-DEGs exhibited positive correlations, and their expressions varied significantly. Additionally, m6A-related genes displayed distinct expression patterns in these subtypes. Immune scores revealed significant differences in Monocyte, Macrophage M1, and Neutrophil populations between the two groups. Expression variations in immune checkpoints, such as CD274, HAVCR2, and PDCD-1LG2, were observed. Although no significant differences were found in immune checkpoint blockade response, the study constructed immune interaction networks involving 15 FR-DEGs and immune cells in each subtype. The significance of these findings lies in unraveling intricate molecular interactions within OC subtypes. Understanding gene correlations, m6A modifications, and immune landscapes provides crucial insights into the disease's complexity. Such knowledge can inform the development of targeted therapies and personalized treatment approaches for distinct molecular subtypes, fostering advancements in OC management.

Among the 15 FR-DEGs were potentially correlated with OC, our attention focused on TRIM46. TRIM46 (Tripartite Motif-Containing Protein 46) is a member of the TRIM family of proteins, which constitutes a large family of E3 ubiquitin ligases that play crucial roles in various biological processes within the cell [33, 34]. TRIM46 contains three key structural domains: the RING, B-box, and coiled-coil domains. The RING domain endows TRIM46 with ubiquitin ligase activity, enabling its participation in the ubiquitination process, which plays a crucial role in regulating protein stability and function [35, 36]. The B-box domain plays a pivotal role in modulating protein-protein interactions and signal transduction. The shared coiled-coil domain, common among other TRIM proteins, is likely associated with subcellular localization and interactions with other proteins [37, 38]. TRIM46 is overexpressed in various cancers and is thought to play a crucial role in regulating cell proliferation, migration, and key signaling pathways [39-41]. However, the expression and function of TRIM46 in OC were rarely reported. In this study, we found that TRIM46 may be a potential regulator in OC progression. Its elevated expression in OC tissues, correlation with diverse stages, and grades of OC, along with its association with poorer overall survival, underscore its significance as a potential prognostic marker. Beyond OC, TRIM46 exhibited wide-

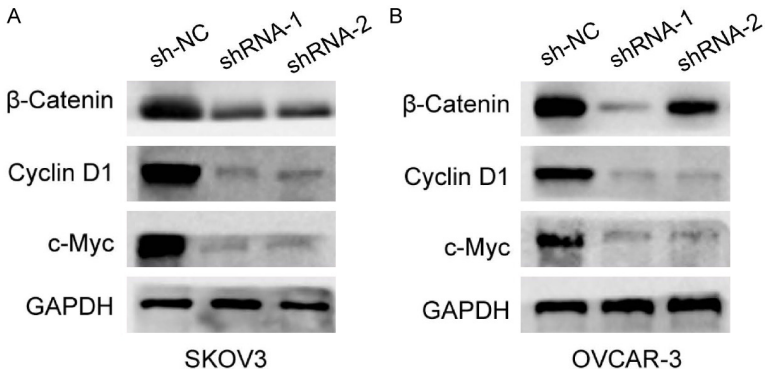

Figure 9. Impact of TRIM46 depletion on Wnt signaling proteins. Western blot assays revealing the protein levels of key Wnt signaling factors, including β-Catenin, cyclin D1, and c-Myc, in (A) SKOV3 and (B) OVCAR-3 cells after TRIM46 depletion.

spread overexpression across various cancer types, implicating its broader role in tumorigenesis. The distinct immune landscapes, immune checkpoint expressions, and responses to immune checkpoint blockade in TRIM46 high and low groups provide valuable insights into its immunomodulatory role. Differentially expressed genes associated with TRIM46 shed light on potential therapeutic targets and biological processes influenced by TRIM46. Moreover, the significant correlations between TRIM46 and metabolism pathways highlight its potential role in modulating cellular metabolic processes. The exploration of the TRIM family in pan-cancers revealed their collective significance in cancer, influencing overall survival and contributing to molecular subtype classifications in OC. This comprehensive analysis enhances our understanding of TRIM46's multifaceted role and emphasizes its potential implications for personalized treatment strategies. More importantly, we performed functional experiments and confirmed that TRIM46 was highly expressed in OC cells and its knockdown distinctly suppressed the proliferation and migration of OC cells. These observations underscore TRIM46 as a potential therapeutic target in OC, suggesting that interventions aimed at modulating TRIM46 expression could influence the progression and metastatic potential of OC cells.

Previously, according to Zhang et al., a regulatory system involving TRIM46 and GPX4 regulates the death of human retinal capillary endothelial cells caused by HG. Cells can protect themselves from high glucose toxicity by blocking this pathway or maintaining GPX4 expression [42]. This research finding has significant biological and clinical implications. First, the identification of a regulatory pathway involving TRIM46 and GPX4 highlights their critical role in modulating iron-dependent cell death in human retinal capillary endothelial cells under high glucose (HG) conditions. This underscores TRIM46's importance in the ferroptosis pathway, particularly in protecting cells from HG-induced damage. Additionally, this discovery offers valuable insights into similar iron-dependent cell death mechanisms that may be involved in other diseases. If the TRIM46-GPX4 pathway proves to be significant in other conditions, targeting this pathway could have broad therapeutic potential across multiple disease areas. This suggests new strategies for treating diseases associated with iron-dependent cell death, such as diabetic retinopathy, offering promise for advancing clinical interventions and improving patient outcomes. In this study, we also explored the relationship between TRIM46 and ferroptosis in OC cells. Bioinformatic analysis using TCGA data revealed a significant positive correlation between TRIM46 and various ferroptosis driver genes in OC samples. Silencing TRIM46 led to increased malondialdehyde (MDA) levels, elevated Fe^{2+} levels, and altered glutathione (GSH) metabolism, indicating a potential role of TRIM46 in regulating ferroptosis in OC cells. Additionally, the study demonstrated a link between TRIM46 and the Wnt signaling pathway, as TRIM46 depletion resulted in decreased levels of key Wnt signaling factors, including β-Catenin, cyclin D1, and c-Myc in OC cancer cells. These findings highlight TRIM46's involvement in ferroptosis regulation and its impact on Wnt signaling in OC cells.

Given the critical role of TRIM46 in OC, developing TRIM46 inhibitors or using RNA interference techniques to disrupt its expression could be an effective therapeutic strategy. Inhibiting TRIM46 expression may slow tumor proliferation and migration, suppress abnormal activation of the Wnt signaling pathway, and influence

ferroptosis mechanisms. This strategy could not only directly inhibit tumor growth but also enhance anticancer effects by inducing ferroptosis. The Wnt signaling pathway is abnormally activated in many cancer types, including OC. In our study, the association between TRIM46 and the Wnt signaling pathway suggests that simultaneously targeting TRIM46 and the Wnt pathway could produce synergistic effects. This combined therapeutic strategy might block tumor cell proliferation and survival through multiple pathways, thereby improving patient outcomes. Further research could explore the potential of TRIM46 as a prognostic marker for ovarian cancer patients and evaluate the therapeutic effects of targeting TRIM46 and the Wnt signaling pathway. In clinical applications, personalized treatment plans based on TRIM46 expression levels may enhance efficacy and reduce side effects. Additionally, combining this approach with other therapies, such as chemotherapy or immunotherapy, could offer more comprehensive treatment options for ovarian cancer patients.

Conclusion

This study, by analyzing the expression and function of TRIM46 in OC, revealed that TRIM46 is highly expressed in OC cells, and its silencing inhibits cell proliferation and migration. Further functional experiments demonstrated that the depletion of TRIM46 induces ferroptosis in OC cells and affects the Wnt signaling pathway. Bioinformatics analysis indicated a significant positive correlation between TRIM46 and various ferroptosis driver genes in OC. Additionally, TRIM46 silencing led to increased malondialdehyde (MDA) levels, elevated Fe^{2+} levels, and altered glutathione (GSH) metabolism in OC cells. Western blot assays showed that TRIM46 suppression significantly decreased the levels of key proteins involved in the Wnt signaling pathway, including β-Catenin, cyclin D1, and c-Myc, in OC cells. Overall, these findings highlight the critical role of TRIM46 in the development of OC, particularly in regulating ferroptosis and the Wnt signaling pathway. The study provides valuable insights into the underlying mechanisms of OC and lays the foundation for potential therapeutic strategies and biomarker discovery.

Acknowledgements

This work was supported by the Chongqing Natural Science Foundation General Project Task Book (No. CSTB2022NSCQ-MSX0264).

Disclosure of conflict of interest

None.

Address correspondence to: Zhigang Wang, Chongqing Key Laboratory of Ultrasound Molecular Imaging, Institute of Ultrasound Imaging, The Second Affiliated Hospital, Chongqing Medical University, No. 76, Linjiang Road, Yuzhong Distinct, Chongqing 400010, China. E-mail: zhigangwang@cqmu.edu.cn; Jing Tang, Department of Ultrasound, Women and Children's Hospital of Chongqing Medical University, No. 120, Longshan Road, Yubei Distinct, Chongqing 401147, China. E-mail: 33070728@qq.com; Ke Yang, Pediatric Research Institute, Ministry of Education Key Laboratory of Child Development and Disorders, Children's Hospital of Chongqing Medical University, Chongqing 400014, China. E-mail: yangke@hospital.cqmu.edu.cn

References

[1] Siegel RL, Miller KD, Fuchs HE and Jemal A. Cancer statistics, 2022. CA Cancer J Clin 2022; 72: 7-33.
[2] Stewart C, Ralyea C and Lockwood S. Ovarian cancer: an integrated review. Semin Oncol Nurs 2019; 35: 151-156.
[3] Morand S, Devanaboyina M, Staats H, Stanbery L and Nemunaitis J. Ovarian cancer immunotherapy and personalized medicine. Int J Mol Sci 2021; 22: 6532.
[4] Lheureux S, Braunstein M and Oza AM. Epithelial ovarian cancer: evolution of management in the era of precision medicine. CA Cancer J Clin 2019; 69: 280-304.
[5] Menon U, Karpinskyj C and Gentry-Maharaj A. Ovarian cancer prevention and screening. Obstet Gynecol 2018; 131: 909-927.
[6] Chen X, Li J, Kang R, Klionsky DJ and Tang D. Ferroptosis: machinery and regulation. Autophagy 2021; 17: 2054-2081.
[7] Tang D, Chen X, Kang R and Kroemer G. Ferroptosis: molecular mechanisms and health implications. Cell Res 2021; 31: 107-125.
[8] Jiang X, Stockwell BR and Conrad M. Ferroptosis: mechanisms, biology and role in disease. Nat Rev Mol Cell Biol 2021; 22: 266-282.
[9] Yang X, Chen Y, Song W, Huang T, Wang Y, Chen Z, Chen F, Liu Y, Wang X, Jiang Y and

Zhang C. Review of the role of ferroptosis in testicular function. Nutrients 2022; 14: 5268.
[10] Zhou B, Liu J, Kang R, Klionsky DJ, Kroemer G and Tang D. Ferroptosis is a type of autophagy-dependent cell death. Semin Cancer Biol 2020; 66: 89-100.
[11] Lei G, Zhuang L and Gan B. Targeting ferroptosis as a vulnerability in cancer. Nat Rev Cancer 2022; 22: 381-396.
[12] Koppula P, Zhuang L and Gan B. Cystine transporter SLC7A11/xCT in cancer: ferroptosis, nutrient dependency, and cancer therapy. Protein Cell 2021; 12: 599-620.
[13] Chen X, Kang R, Kroemer G and Tang D. Broadening horizons: the role of ferroptosis in cancer. Nat Rev Clin Oncol 2021; 18: 280-296.
[14] Tong X, Tang R, Xiao M, Xu J, Wang W, Zhang B, Liu J, Yu X and Shi S. Targeting cell death pathways for cancer therapy: recent developments in necroptosis, pyroptosis, ferroptosis, and cuproptosis research. J Hematol Oncol 2022; 15: 174.
[15] Xuan Y, Wang H, Yung MM, Chen F, Chan WS, Chan YS, Tsui SK, Ngan HY, Chan KK and Chan DW. SCD1/FADS2 fatty acid desaturases equipoise lipid metabolic activity and redox-driven ferroptosis in ascites-derived ovarian cancer cells. Theranostics 2022; 12: 3534-3552.
[16] Zhang C and Liu N. Ferroptosis, necroptosis, and pyroptosis in the occurrence and development of ovarian cancer. Front Immunol 2022; 13: 920059.
[17] Wang Y, Zhao G, Condello S, Huang H, Cardenas H, Tanner EJ, Wei J, Ji Y, Li J, Tan Y, Davuluri RV, Peter ME, Cheng JX and Matei D. Frizzled-7 identifies platinum-tolerant ovarian cancer cells susceptible to ferroptosis. Cancer Res 2021; 81: 384-399.
[18] Xiao Y, Bi M, Guo H and Li M. Multi-omics approaches for biomarker discovery in early ovarian cancer diagnosis. EBioMedicine 2022; 79: 104001.
[19] Dochez V, Caillon H, Vaucel E, Dimet J, Winer N and Ducarme G. Biomarkers and algorithms for diagnosis of ovarian cancer: CA125, HE4, RMI and ROMA, a review. J Ovarian Res 2019; 12: 28.
[20] Nebgen DR, Lu KH and Bast RC Jr. Novel approaches to ovarian cancer screening. Curr Oncol Rep 2019; 21: 75.
[21] Lisio MA, Fu L, Goyeneche A, Gao ZH and Telleria C. High-grade serous ovarian cancer: basic sciences, clinical and therapeutic standpoints. Int J Mol Sci 2019; 20: 952.
[22] Akram F, Atique N, Haq IU, Ahmed Z, Jabbar Z, Nawaz A, Aqeel A and Akram R. MicroRNA, a promising biomarker for breast and ovarian cancer: a review. Curr Protein Pept Sci 2021; 22: 599-619.
[23] Chandra A, Pius C, Nabeel M, Nair M, Vishwanatha JK, Ahmad S and Basha R. Ovarian cancer: current status and strategies for improving therapeutic outcomes. Cancer Med 2019; 8: 7018-7031.
[24] Ford CE, Werner B, Hacker NF and Warton K. The untapped potential of ascites in ovarian cancer research and treatment. Br J Cancer 2020; 123: 9-16.
[25] Zhang C, Liu X, Jin S, Chen Y and Guo R. Ferroptosis in cancer therapy: a novel approach to reversing drug resistance. Mol Cancer 2022; 21: 47.
[26] Mou Y, Wang J, Wu J, He D, Zhang C, Duan C and Li B. Ferroptosis, a new form of cell death: opportunities and challenges in cancer. J Hematol Oncol 2019; 12: 34.
[27] Chen X, Kang R, Kroemer G and Tang D. Ferroptosis in infection, inflammation, and immunity. J Exp Med 2021; 218: e20210518.
[28] Liu J, Kang R and Tang D. Signaling pathways and defense mechanisms of ferroptosis. FEBS J 2022; 289: 7038-7050.
[29] Wu X, Li Y, Zhang S and Zhou X. Ferroptosis as a novel therapeutic target for cardiovascular disease. Theranostics 2021; 11: 3052-3059.
[30] Gao J, Wang Q, Tang YD, Zhai J, Hu W and Zheng C. When ferroptosis meets pathogenic infections. Trends Microbiol 2023; 31: 468-479.
[31] Qiu Y, Cao Y, Cao W, Jia Y and Lu N. The application of ferroptosis in diseases. Pharmacol Res 2020; 159: 104919.
[32] Li D and Li Y. The interaction between ferroptosis and lipid metabolism in cancer. Signal Transduct Target Ther 2020; 5: 108.
[33] Valencia-Sanchez C, Knight AM, Hammami MB, Guo Y, Mills JR, Kryzer TJ, Piquet AL, Amin A, Heinzelmann M, Lucchinetti CF, Lennon VA, McKeon A, Pittock SJ and Dubey D. Characterisation of TRIM46 autoantibody-associated paraneoplastic neurological syndrome. J Neurol Neurosurg Psychiatry 2022; 93: 196-200.
[34] Harterink M, Vocking K, Pan X, Soriano Jerez EM, Slenders L, Fréal A, Tas RP, van de Wetering WJ, Timmer K, Motshagen J, van Beuningen SFB, Kapitein LC, Geerts WJC, Post JA and Hoogenraad CC. TRIM46 organizes microtubule fasciculation in the axon initial segment. J Neurosci 2019; 39: 4864-4873.
[35] Shen H, Gong Q, Zhang J, Wang H, Qiu Q, Zhang J and Luo D. TRIM46 aggravated high glucose-induced hyper permeability and inflammatory response in human retinal capillary endothelial cells by promoting IκBα ubiquitination. Eye Vis (Lond) 2022; 9: 35.
[36] Jung J, Kim J, Huh TL and Rhee M. Trim46 contributes to the midbrain development via Sonic Hedgehog signaling pathway in zebrafish em-

bryos. Anim Cells Syst (Seoul) 2021; 25: 56-64.
[37] van Beuningen SFB, Will L, Harterink M, Chazeau A, van Battum EY, Frias CP, Franker MAM, Katrukha EA, Stucchi R, Vocking K, Antunes AT, Slenders L, Doulkeridou S, Sillevis Smitt P, Altelaar AFM, Post JA, Akhmanova A, Pasterkamp RJ, Kapitein LC, de Graaff E and Hoogenraad CC. TRIM46 controls neuronal polarity and axon specification by driving the formation of parallel microtubule arrays. Neuron 2015; 88: 1208-1226.
[38] Guan F, Gao S, Sheng H, Ma Y, Chen W, Qi X, Zhang X, Gao X, Pang S, Zhang L and Zhang L. Trim46 knockout impaired neuronal architecture and caused hypoactive behavior in rats. Dev Dyn 2024; 253: 659-676.
[39] Tantai J, Pan X, Chen Y, Shen Y and Ji C. TRIM46 activates AKT/HK2 signaling by modifying PHLPP2 ubiquitylation to promote glycolysis and chemoresistance of lung cancer cells. Cell Death Dis 2022; 13: 285.
[40] Zhang L, Li X, Dong W, Sun C, Guo D and Zhang L. Mmu-miR-1894-3p inhibits cell proliferation and migration of breast cancer cells by targeting Trim46. Int J Mol Sci 2016; 17: 609.
[41] Kannan K, Kordestani GK, Galagoda A, Coarfa C and Yen L. Aberrant MUC1-TRIM46-KRTCAP2 chimeric RNAs in high-grade serous ovarian carcinoma. Cancers (Basel) 2015; 7: 2083-2093.
[42] Zhang J, Qiu Q, Wang H, Chen C and Luo D. TRIM46 contributes to high glucose-induced ferroptosis and cell growth inhibition in human retinal capillary endothelial cells by facilitating GPX4 ubiquitination. Exp Cell Res 2021; 407: 112800.

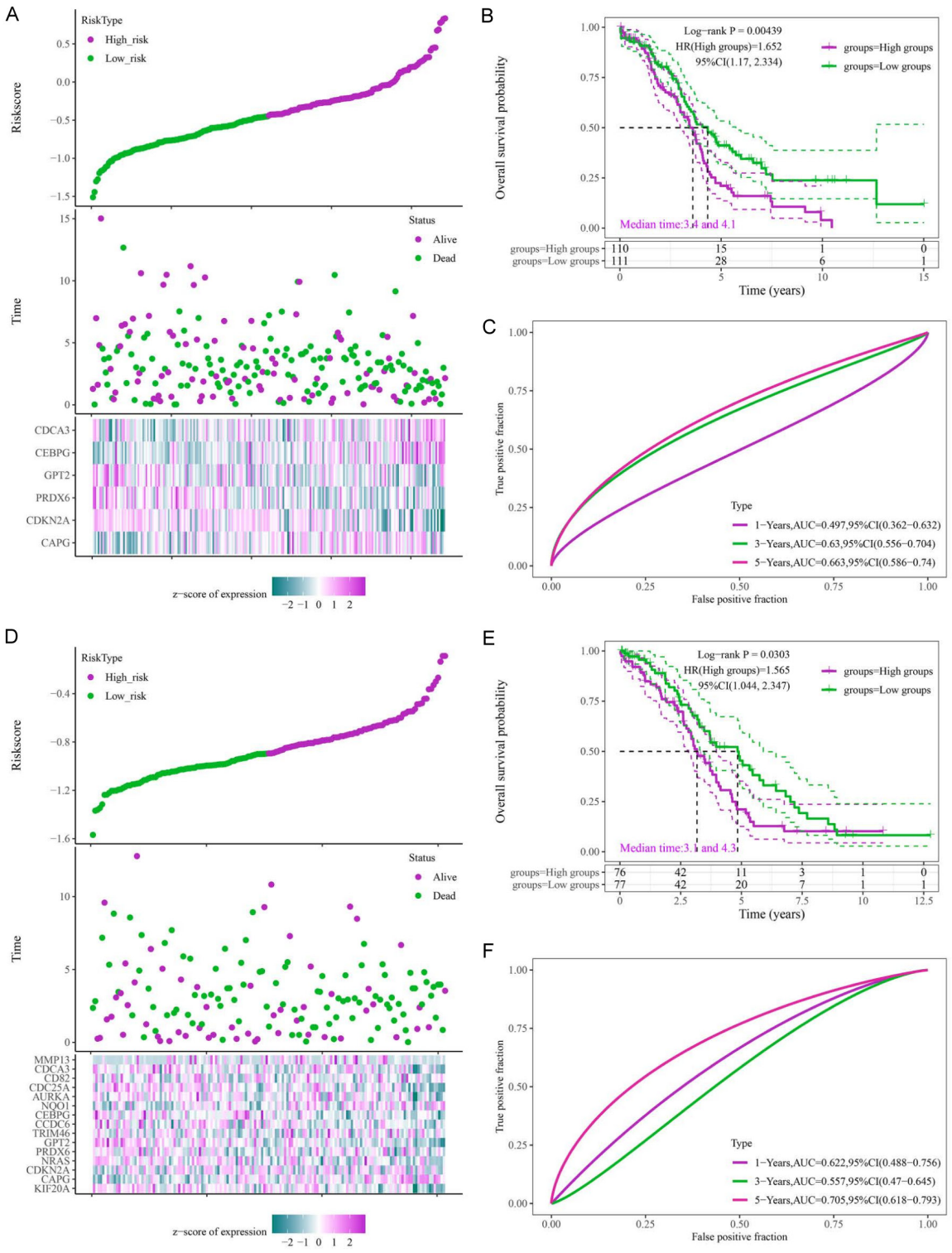

Figure S1. Construction and evaluation of prognostic models for OV molecular subtypes based on 15 ferroptosis-related differentially expressed genes (FR-DEGs). A. Risk score model for molecular subtype group 1 (C1). Utilization of the "Step" method to predict the optimal prognostic model for group 1 (221 OV samples). B. Kaplan-Meier analysis for group 1 prognostic model. C. Time-dependent receiver operating characteristic (ROC) analysis for group 1 prognostic model. D. Risk score model for molecular subtype group 2 (C2). application of the "Step" method to predict the optimal prognostic model for group 2 (155 OV samples). E. Kaplan-Meier analysis for group 2 prognostic model. F. Time-dependent ROC analysis for group 2 prognostic model.

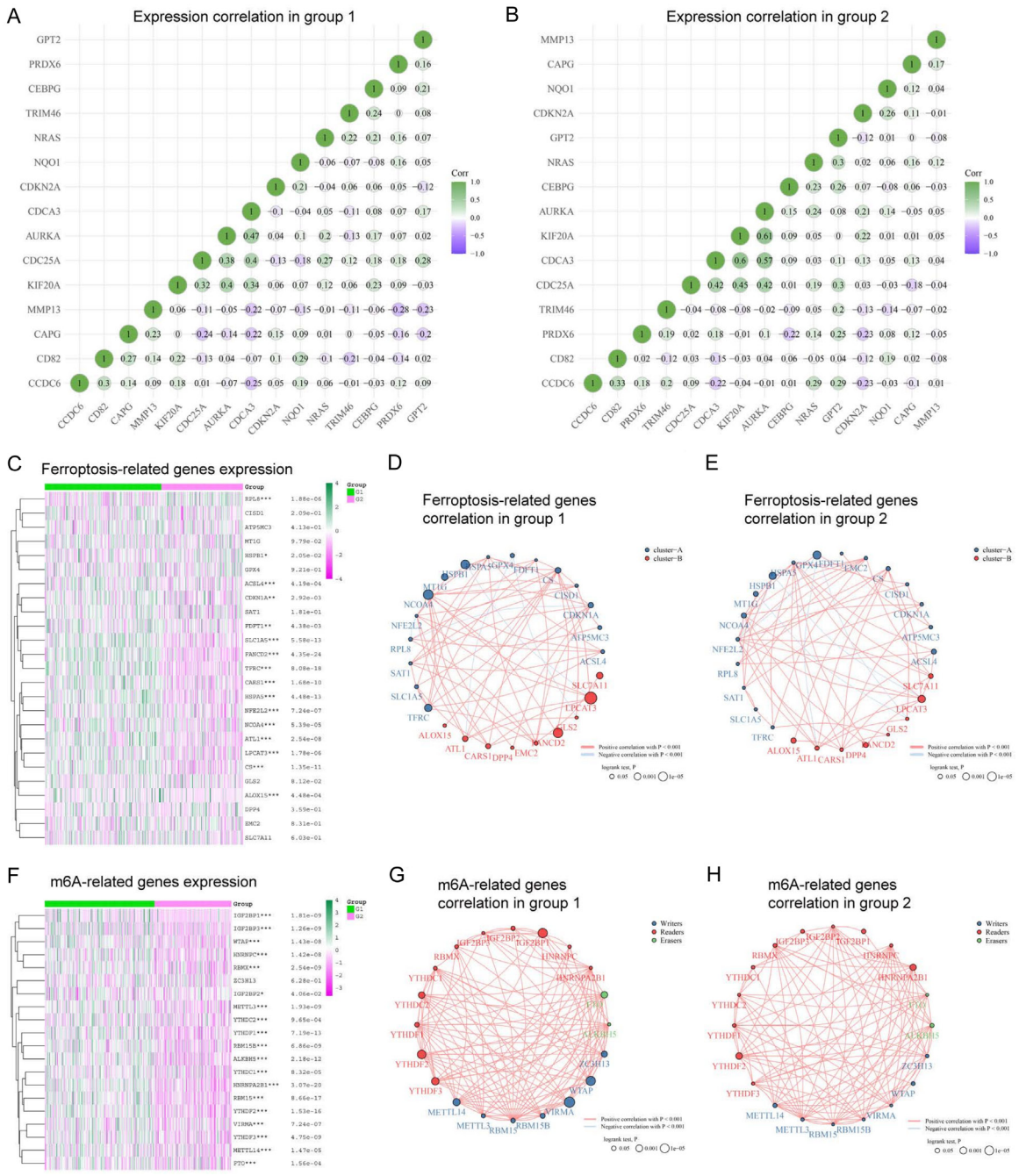

Figure S2. Gene correlation analysis in two OV molecular subtypes. A. Gene correlation analysis in group 1. B. Gene correlation analysis in group 2. C. Heatmap of ferroptosis-related gene expression in both subtypes. D. Ferroptosis-related gene correlation in group 1. E. Ferroptosis-related gene correlation in group 2. F. m6A-related gene expression in both subtypes. G. m6A-related gene correlation in group 1. H. Correlation analysis of m6A-related genes in group 2.

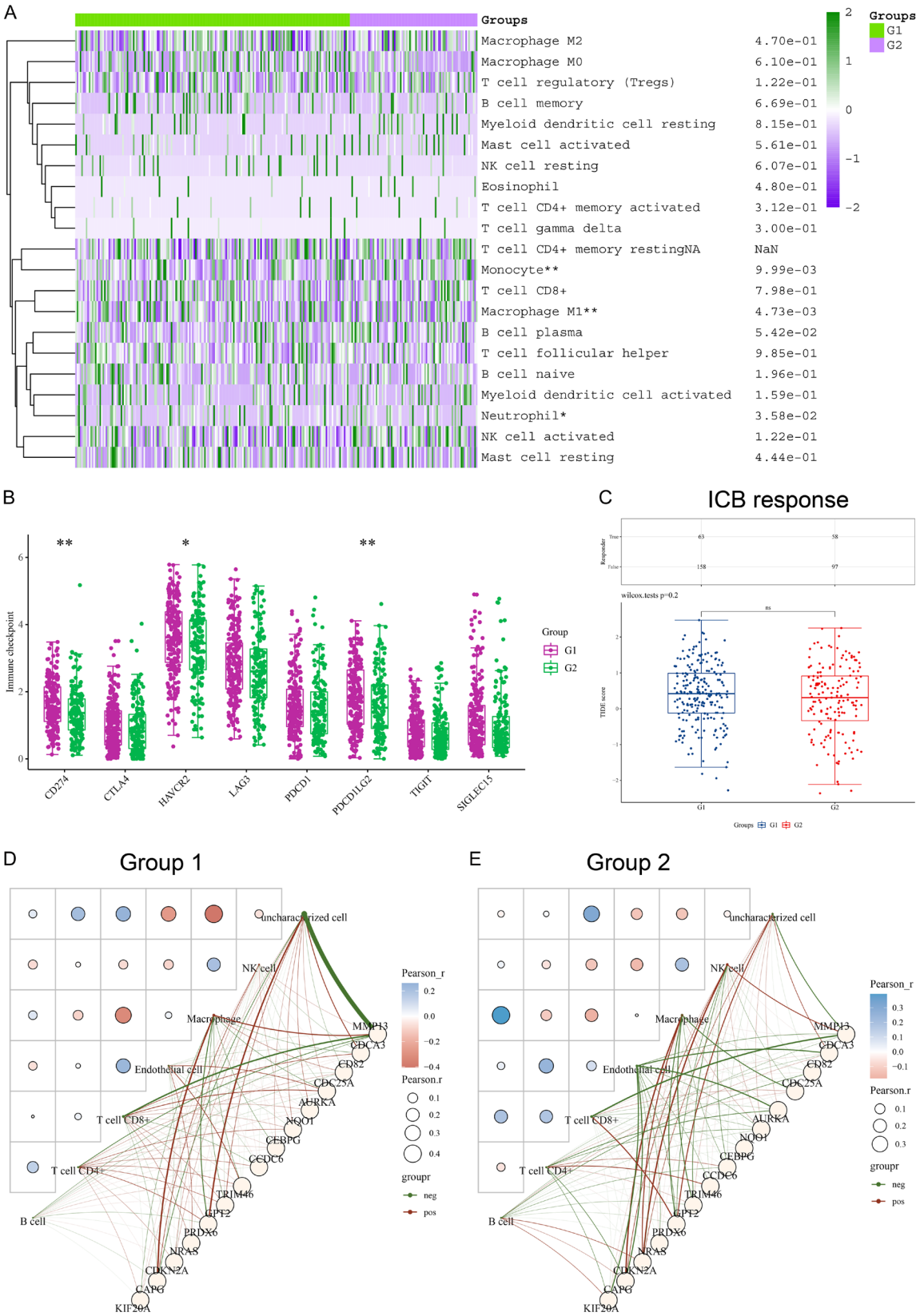

Figure S3. Immune-related analyses in two molecular subtypes of OV. A. Immune scores evaluation using CIBERSORT. B. Analysis of immune checkpoint expression, including CD274, HAVCR2, and PDCD1LG2, in group 1 and

group 2 molecular subtypes of OV. C. Estimation of the immune checkpoint blockade (ICB) response in group 1 and group 2 molecular subtypes. D. Construction of the immune interacting network involving 15 FR-DEGs and immune cells (B cell, T cell CD4+, T cell CD8+, Endothelial cell, Macrophage, NK cell) in group 1 molecular subtype of OV. E. Immune interacting network in group 2.

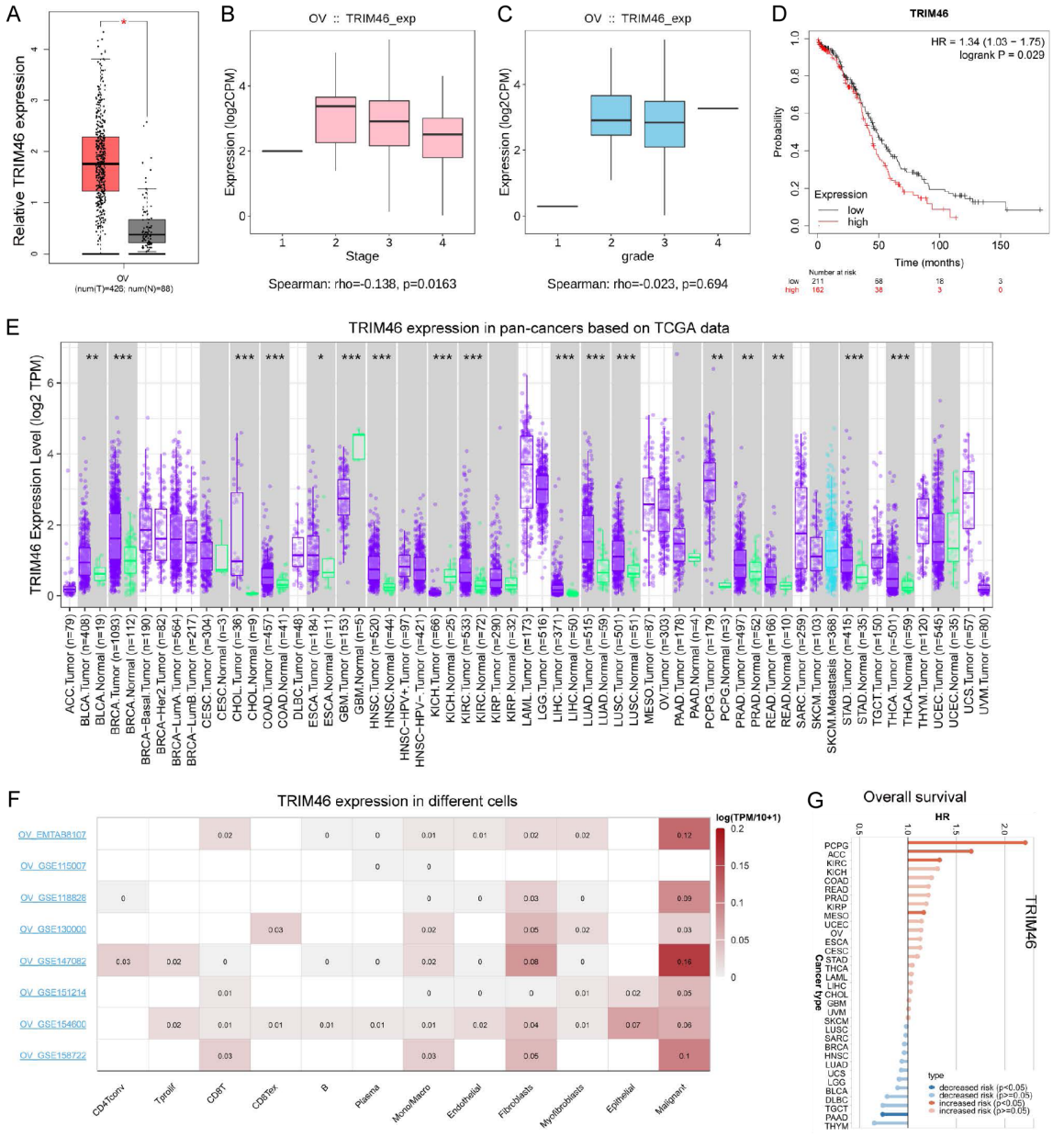

Figure S4. Expression and survival analyses of TRIM46 in pan-cancers. A. Investigation of TRIM46 expression in OV samples compared to normal tissues, based on data from the GEPIA database. B. TRIM46 expression in different stages of OV. C. TRIM46 expression in different grades of OV. D. Kaplan-Meier plot demonstrating the overall survival of OV patients with high and low TRIM46 expression levels, based on the Kaplan-Meier plotter database. E. TRIM46 expression in various cancer types. F. TRIM46 expression in different cells of OV tissues. G. Kaplan-Meier analysis illustrating the overall survival of patients with high and low TRIM46 expression in pan-cancers, based on the TISCH2 database.

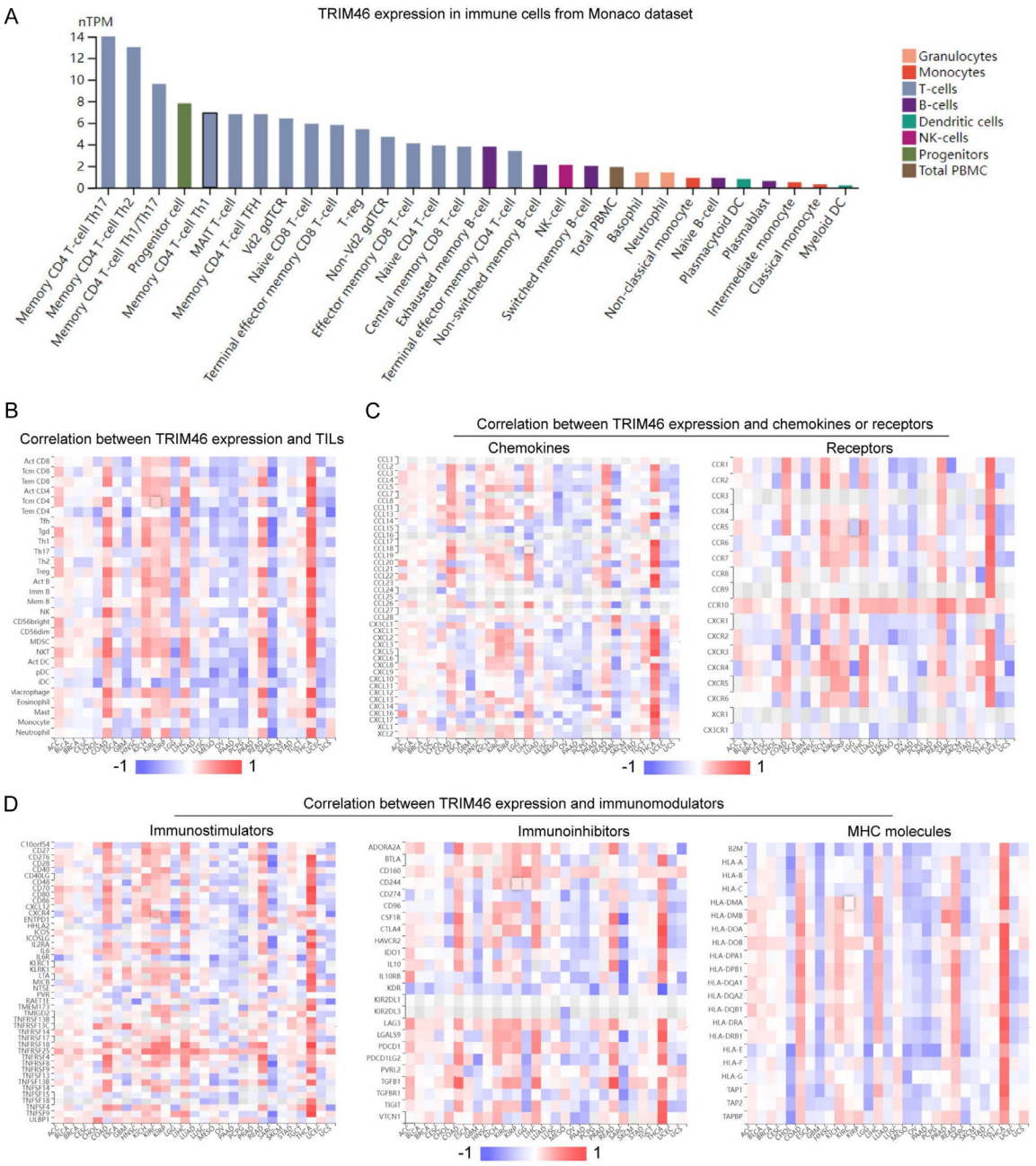

Figure S5. Immune-related analyses of TRIM46 in pan-cancers. A. Analysis of TRIM46 expression in various immune cells from healthy donors, revealing higher expression in memory CD4 T-cell Th17, memory CD4 T-cell Th2, and memory CD4 T-cell Th1/Th17, based on the human protein atlas data from Monaco dataset. B. Correlation between TRIM46 expression and tumor infiltrating lymphocytes (TILs). C. Correlation between TRIM46 expression and chemokines/receptors. D. Correlation between TRIM46 expression and immunomodulators.

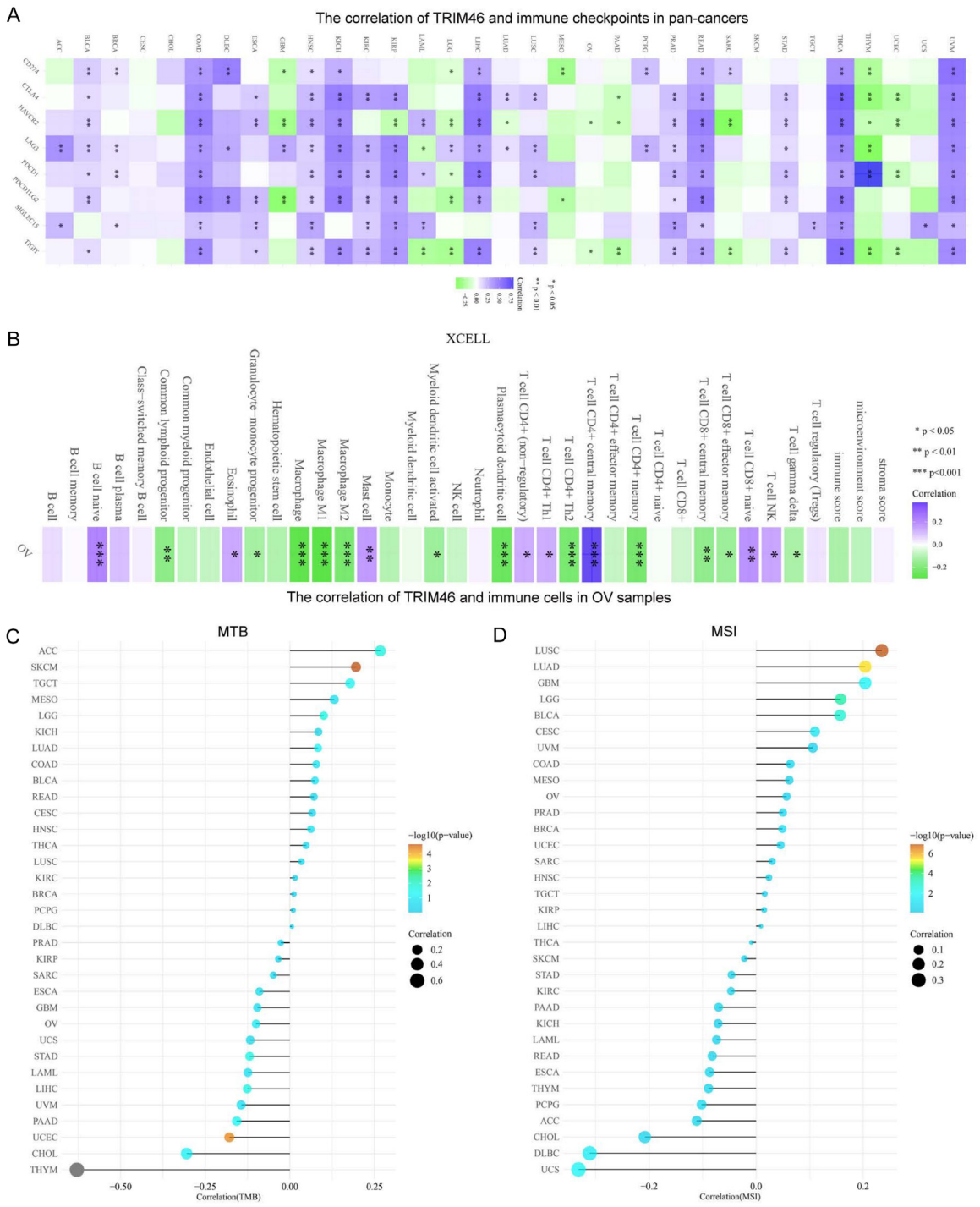

Figure S6. Further immune-related analyses of TRIM46 in pan-cancers. A. Heatmap showing the correlation between TRIM46 expression and immune checkpoint-related genes in various cancer types. B. Correlation between TRIM46 and immune cells in OV. C. Investigation of the correlation between TRIM46 expression and tumor mutation burden (TMB) in pan-cancers, indicating significant correlations in more than half of the TCGA cancer types. D. Correlation between TRIM46 and microsatellite instability (MSI).

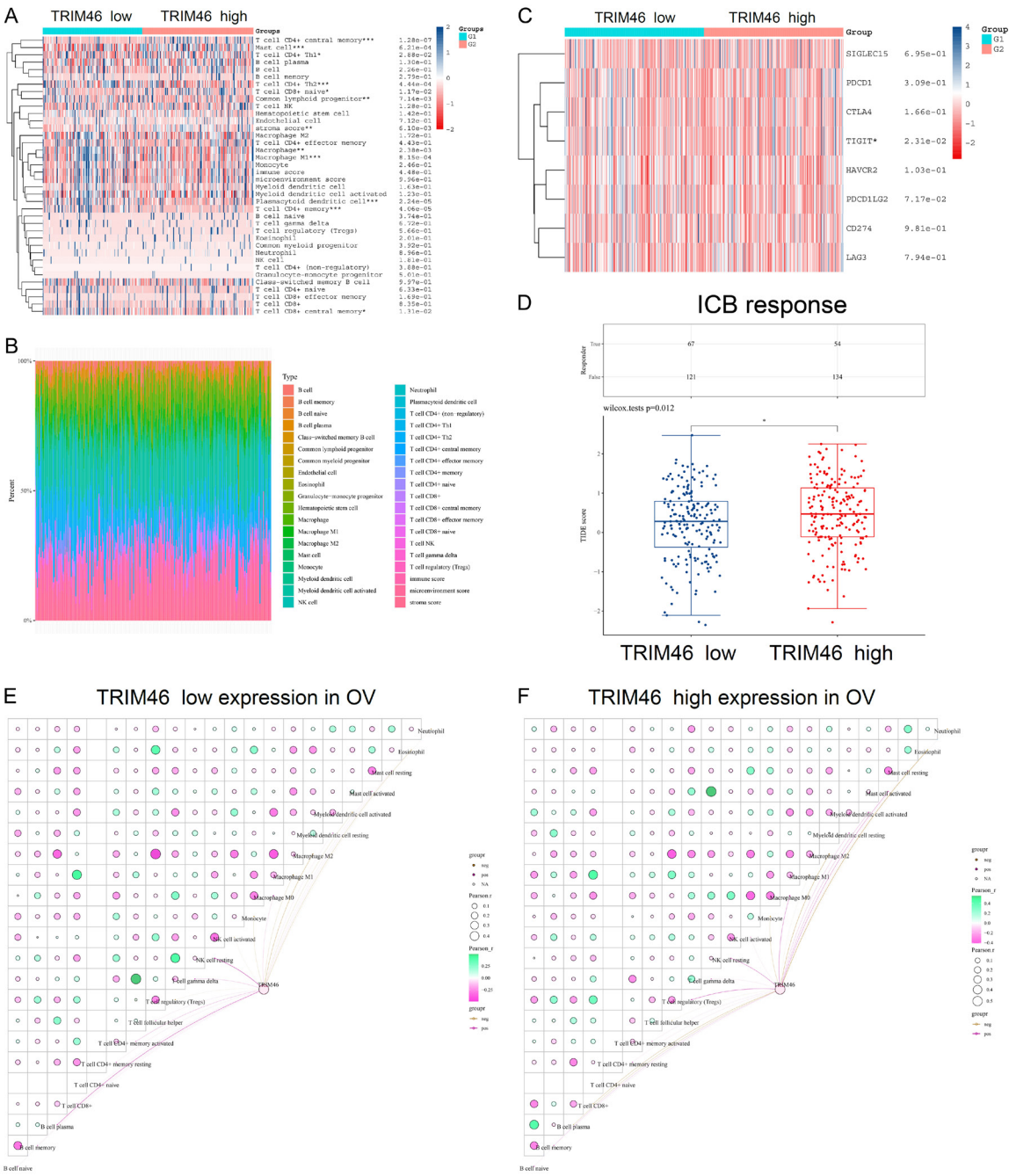

Figure S7. Immune analyses in TRIM46 high and low groups of OV. A. Comparison of immune cell composition differences between TRIM46 high and low groups in OV samples, using the CIBERSORT algorithm. B. Distribution of 22 types of immune cells in TRIM46 high and low groups. C. Expression of immune checkpoints in TRIM46 high and low groups. D. Immune checkpoint blockade (ICB) response in TRIM46 high and low groups. E. Construction of the immune interacting network involving TRIM46 and immune cells (B cell, T cell CD4+, T cell CD8+, Endothelial cell, Macrophage, NK cell) in TRIM46 low group of OV. F. Immune interacting network in TRIM46 high group.

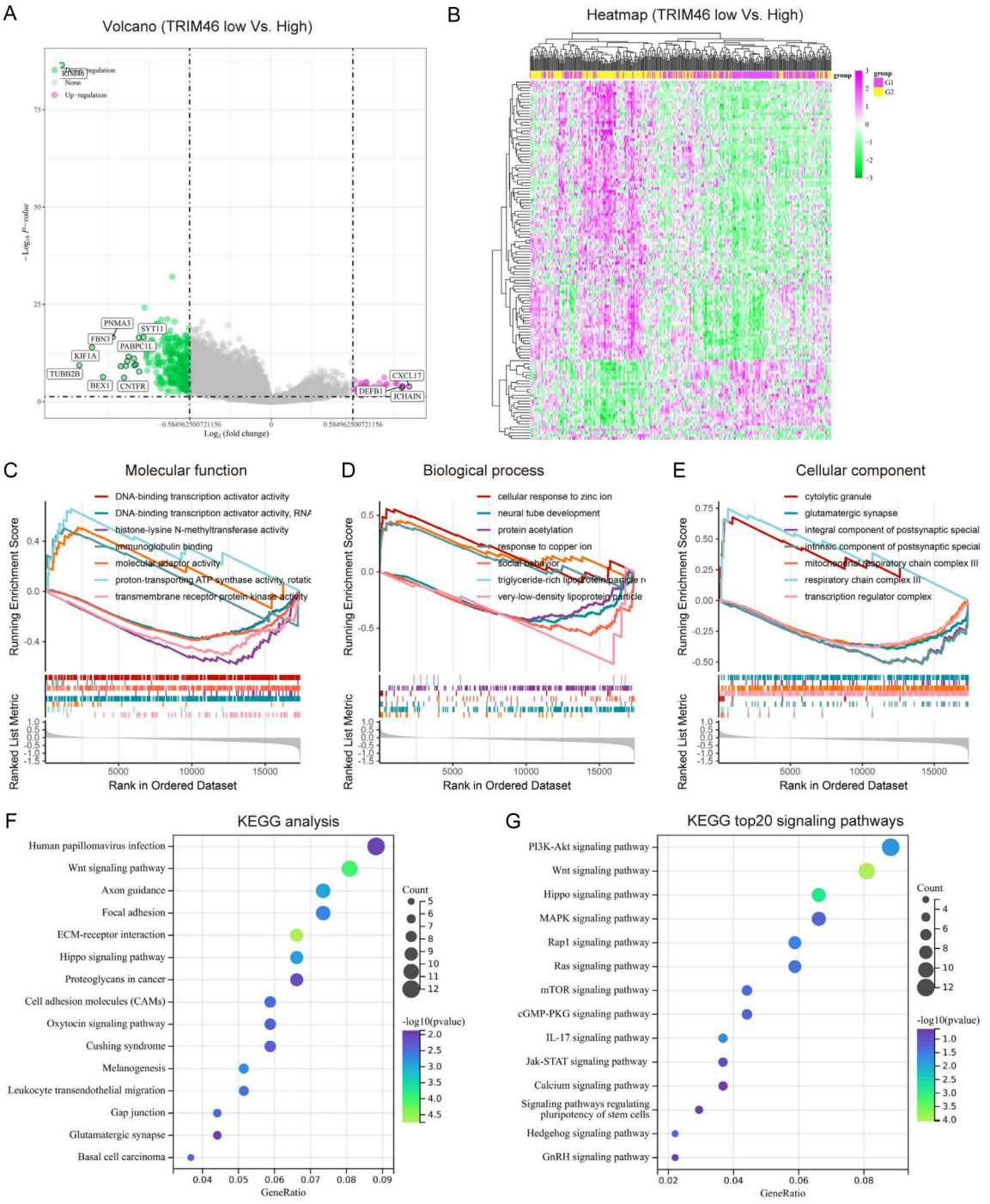

Figure S8. A, B. DEGs analysis in TRIM46 low and high groups. C-E. GO analysis of DEGs. F. KEGG pathway analysis of DEGs. G. Top 20 signaling pathways from KEGG analysis.

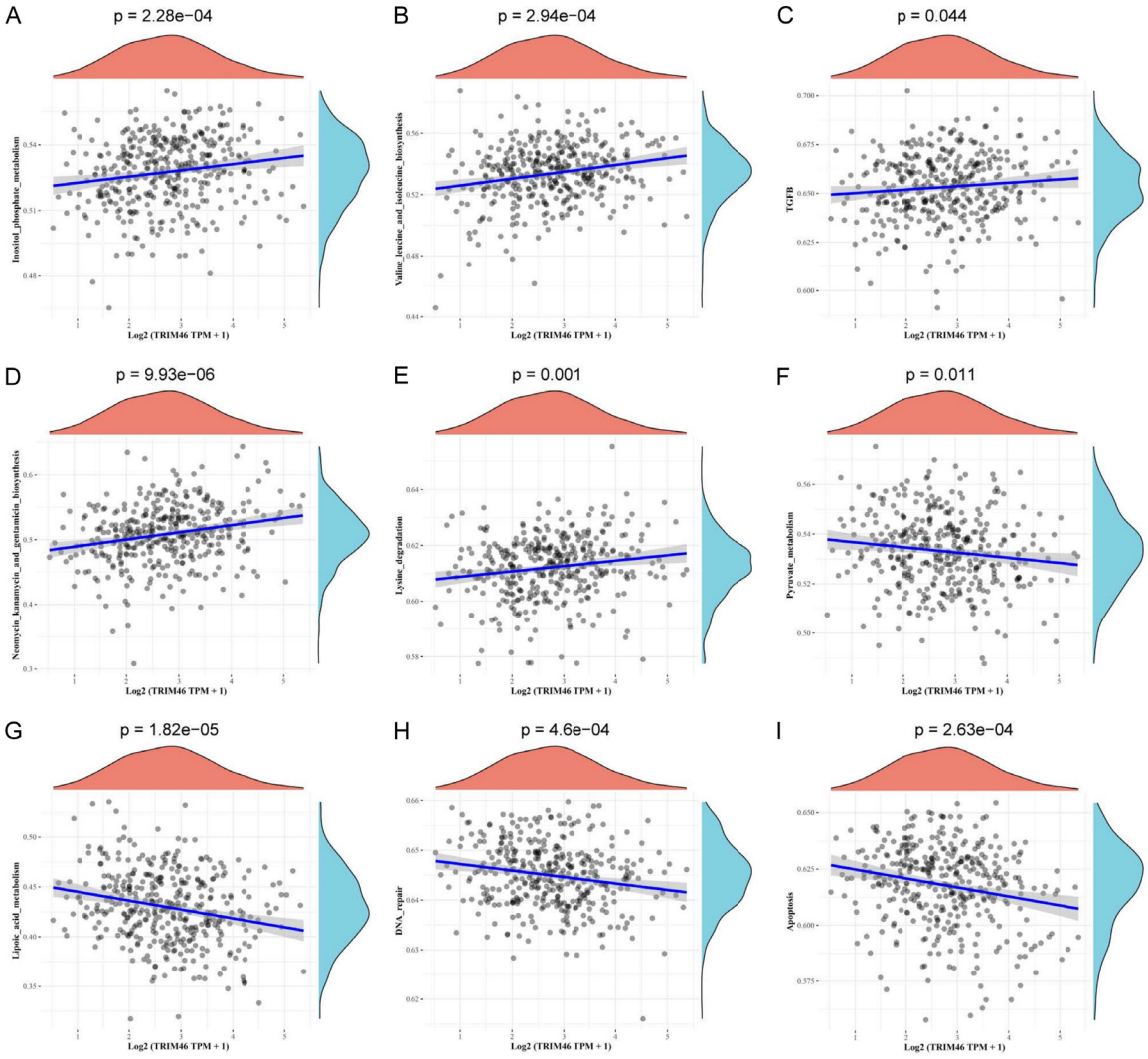

Figure S9. Correlation of TRIM46 with metabolism pathways, including (A) Inositol Phosphate Metabolism, Valine, (B) Leucine, and Isoleucine Biosynthesis, (C) TGFB (Transforming Growth Factor Beta) Pathway, (D) Neomycin, Kanamycin, and Gentamicin Biosynthesis, (E) Lysine Degradation, (F) Pyruvate Metabolism, (G) Lipoic Acid Metabolism, (H) DNA Repair Pathway and (I) Apoptosis Pathway.

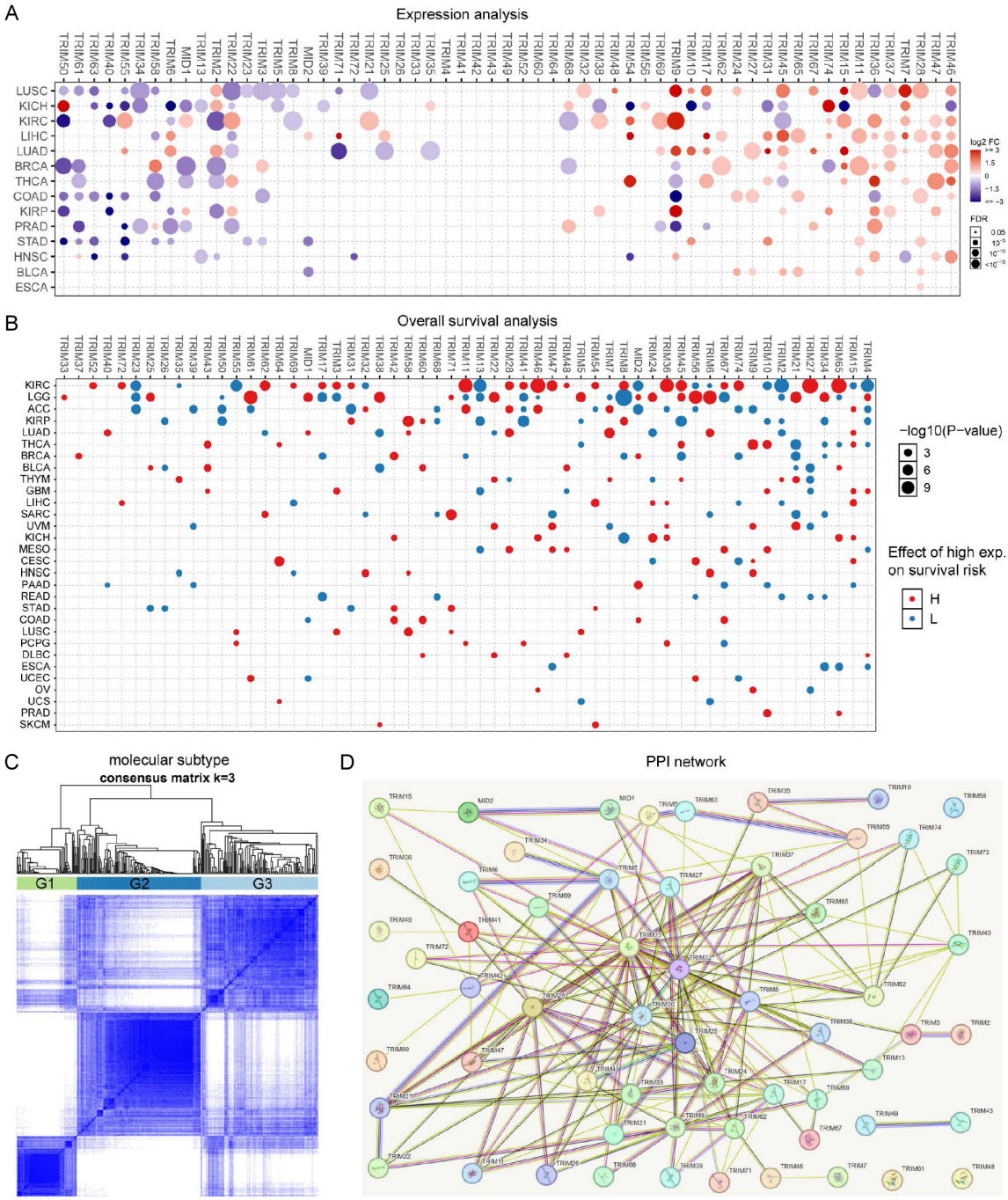

Figure S10. The expression, survival, molecular subtype classification and PPI network of TRIM family in pan-cancers. A. Expression analysis of TRIM family members in pan-cancers. B. Overall survival analysis of TRIM family members in pan-cancers. C. Identification of molecular subtypes in OV using TRIM family members. D. Construction of the protein-protein interaction (PPI) network of TRIM family members using the STRING database.